UNIVERSITY OF CALIFORNIA
Santa Barbara

Search For New Physics Coupling to the Z Boson

A Dissertation submitted in partial satisfaction
of the requirements for the degree of

Doctor of Philosophy

in

Physics

by

Adam Liddle Scott

Committee in Charge:

Professor David Stuart, Chair

Professor Claudio Campagnari

Professor Mark Srednicki

June 2007

The Dissertation of
Adam Liddle Scott is approved:

Professor Claudio Campagnari

Professor Mark Srednicki

Professor David Stuart, Committee Chairperson

June 2007

Search For New Physics Coupling to the Z Boson

by

Adam Liddle Scott

I couldn't decide to whom I should dedicate this, so... I dedicate this work to everybody!

Acknowledgements

But I acknowledge nobody, except the person that wrote this thesis. Myself.

I hope you understand that I am joking. Anything anybody on Earth does is really a team effort. I would like to acknowledge that throughout my work on this thesis (and indeed throughout my entire life) I have received the support of an uncounted number of humans, living and dead. Listing them all by name is, of course, an impossible task. I will instead list them by category. My family and friends, who made sure my basic survival needs were met, supported me financially and emotionally, educated me, and generally kept me sane. My pre-undergraduate, undergraduate, and graduate school colleagues and teachers, whose total aggregate effort taught me everything I know. All of my fellow collaborators who lay the foundations for my (and all) analyses with their efforts to understand our detector and accelerator and everything else, and who make sure there is money for this work. The governments and their employees (of the US and all of the collaborating countries of my and other experiments), who (despite sometimes frustrating everyone) recognize the need for these types of research, and provide the money for it. The people that work within these

countries that give their money to the governments in taxes. These same people, plus many others, in the various economies around the world that help provide me with the basic survival needs (e.g., food and shelter), the infrastructure, and the entertainment that I want/need to live, all in exchange for a relatively small amount a money that they themselves provided to the governments who then distributed it through various institutions until some of it finally made its way to me. (Human social structures are so delightfully circular and complex). And the humans that lived before those currently alive that provided the foundations of all of our knowledge and everything else.

Abstract

Search For New Physics Coupling to the Z Boson

Adam Liddle Scott

We present the results of two searches for new particles that couple Z bosons in $p\bar{p}$ collisions at $\sqrt{s} = 1.96$ TeV using the Collider Detector at Fermilab (CDF). In the first, we search for a long-lived parent of the Z boson using a data sample with a luminosity of 163 pb^{-1}. Finding no significant excess above background, we set a limit on a fourth generation model as a function of mass and lifetime. In the second, we search for a particle that decays to a Z boson in conjunction with jets using a data sample with a luminosity of 1.06 fb^{-1}. Finding no significant excess above background, we set a limit on a fourth generation model as a function of mass.

Contents

Chapter 1

Introduction

Dear Reader,

Thank you for your interest in my thesis. I hope you find it informative. Its purpose is to document the work of my graduate career, to describe the reasons for doing the work I did, the results of doing the work I did, and what I have learned in the process that others may find useful.

Where shall I start? Well, the first task of any thesis is certainly to describe the current state of whatever field the thesis concerns. As such, I will begin by giving a general overview of the field of particle physics. After this groundwork has been laid, we[1] will segue naturally into the motivations for doing the work

[1] I'll be using "we," "our," and "us" a lot in this thesis. When I do, I am not using the "royal we," referring to myself alone. Rather, I am referring to either (1) you (the reader) and me, or (2) my collaborators and me.

I did, then on to the tools that I used (the accelerator called the "Tevatron" and the detector called "CDF"), and then finally on to the specific details of the analysis that I did. But enough chit-chat, let's get going!

1.1 Theoretical Picture

When asked to describe the current theoretical landscape in the field of particle physics, two words will arise first in the mind of practically any particle physicist: standard model. This is a theory that describes the behavior of elementary particles and their interactions, and makes predictions for all observable quantities. The standard model is the curse tormenting nearly all particle physicists today. It is our curse because of the following facts:

- It is inelegant and arbitrary—there is no apparent reason why it has the particle content that it has, there is no apparent reason why its parameters have the values they have, and there is no apparent reason why it has the gauge symmetry that it has.

- It predicts an infinite value for the Higgs mass when calculated to all orders in perturbation theory.

- Since it does not incorporate gravity, it must break down at some high energy/short distance as quantum gravitational effects become important.

- It is able to predict with frustrating agreement nearly[2] all observations to date.

This last fact has been confirmed time and again using an uncounted amount of money and person-hours, while the motivation to spend that money and person-hours is perhaps summarized by the first three facts.

I (along with the entire particle physics community) wish to understand the solutions to these problems. I (and many many others) attempt to do so from the experimental side, searching for the experimental consequences of new theories that solve these problems, hoping to find deviations from predictions made by the standard model.

Since these problems relate to behavior at distance scales unexplored by previous measurements, perhaps the most natural way to find their solutions is to construct a device that can probe these short distances. As the wavelengths of particles are related to their energy via $E = h\nu = hc/\lambda$, probing shorter distances inevitably amounts to probing higher energies. The device we are describing is called a "particle accelerator", a device that (not surprisingly) ac-

[2]I say "nearly" because neutrinos are now known to have mass. This is not possible in the standard model, which only has left-handed neutrino fields. But, the standard model can easily accommodate massive neutrinos by adding right-handed neutrino fields. Many would favor this approach; those that oppose this proposal do so because they oppose introducing new unobserved particles, especially those that are unobservable. That is, these added fields would not interact via the electroweak or the strong force, so confirming their existence would almost certainly be impossible.

celerates particles into high energy beams and collides them. The problem-laden standard model predicts certain behavior of these collisions, while new theories and structures that only become apparent at short distances predict different behavior. We thus examine these collisions, hoping to find unexpected results.

In order to understand the problems described above, one must understand the standard model. I will not be describing the standard model with the sufficient detail required to teach it to those who are not already familiar with it. Please see the references for a full description [1]. Instead of an in-depth discussion, I give a brief overview of the standard model that serves the purposes required in this chapter.

The standard model consists of the following:

- The gauge group $SU(3) \times SU(2) \times U(1)$.
- Gauge fields that form the derivative invariant with respect to the $SU(3) \times SU(2) \times U(1)$ gauge group transformations (the "covariant derivative"): 8 gauge fields for the 8 generators of $SU(3)$, 3 gauge fields for the 3 generators of $SU(2)$, and 1 gauge field for the generator of $U(1)$.
- A set of fermion fields belonging to specific representations of each of the gauge group factors (each fermion field belongs to specific representations

of each of the $SU(3)$, $SU(2)$, and $U(1)$). There are three identical copies of this set of fields, each known as a "generation."

- A complex scalar field (the Higgs field) belonging to specific representations of each of the group factors, and with a non-zero vacuum expectation value.

- A Lagrangian with all possible terms that are both renormalizable and invariant with respect to a $SU(3) \times SU(2) \times U(1)$ gauge transformation. Appropriate terms have coefficients in front of them (and are free parameters in the model).

Given this Lagrangian (and the values of its parameters), one then uses the techniques of quantum field theory to calculate any observable one desires (at least in principle).

Now that we have a (quite short) description of the standard model, I am able to describe each of its problems further, as well as possible solutions to these problems.

1.1.1 The Arbitrariness Problem

As one can easily see from the above description, a disappointing feature of the standard model is its *ad hoc* nature. There are many free parameters only determined by experiment (18 of them, see [2]). No reason is given for three

generations of particles (identical except for their mass); no reason is given for the structure of a single generation. The origin of the gauge symmetry that it respects, $SU(3) \times SU(2) \times U(1)$, is completely unknown.

Natural solutions to these problems are found in Grand Unified Theories (GUTs) [3]. In GUTs, gauge groups of larger size (or "rank" in group theory language) are postulated. These higher rank groups are theorized to reduce to the gauge group of the standard model through a symmetry breaking mechanism, deriving the observed $SU(3) \times SU(2) \times U(1)$ gauge group from the higher rank gauge group. In the process, this method attempts to explain the observed particle spectrum and the relations between the observed coupling constants. However, it is difficult to reproduce the standard model's particle content via this method without extra non-standard model fermions arising in the theory [3]. If the standard model is truly just the low energy behavior of a GUT, then discovering such additional particles can determine the structure of the GUT, thereby illuminating the standard model's seemingly arbitrary nature.

1.1.2 The Higgs Mass Problem

When making predictions with the standard model, one typically uses the techniques in quantum field theory to calculate the lowest order terms in a perturbation series to perform calculations. To obtain exact predictions, one

must calculate all orders of the perturbation series and perform an infinite sum. In particular, one must do this to calculate the Higgs mass. When doing so, one finds that higher-order diagrams contributing to the propagator involve loops of fermions that give infinite terms, resulting in an infinite Higgs boson mass[3]. As the Higgs boson has not yet been discovered, one might consider revising the Higgs sector of the standard model to resolve this problem. However, the standard model's *a priori* prediction of the W and Z bosons' existence (as well as predicting their correct masses) leads one to believe the current Higgs sector is correct.

The theory called "supersymmetry" (SUSY) offers a different solution to this problem [6]. The symmetry of SUSY is a boson-fermion symmetry. For every fermion (the quarks and leptons) it postulates the existence of a boson "super-partner" (the squarks and sleptons), a particle with identical properties, except for a different spin; for every boson (the W, Z, photon, gluon, and Higgs) it postulates the existence of a fermion super-partner (the wino, zino, photino, gluino, and higgsino). It is perhaps necessary to mention that while the properties of

[3]Some would say the the Higgs mass is not predicted to be infinity as the momentum integral should not be carried to infinity, but to some large cutoff equal to the scale at which new physics turns on, resulting in a non-infinite but extremely large Higgs mass of order the cutoff. This still results in an inconsistency, as the Higgs mass is related at higher orders to the masses of the W boson and the t quark [4]. This inconsistency can be avoided if one fine tunes the Higgs bare mass to one part in 10^{17} [5]. However, in all of this, one assumes that there is physics beyond the standard model at the scale of the momentum cutoff. So, even if we allow this fine-tuning, we are still admitting that the standard model is incomplete.

the boson-fermion pairs are identical, the mass of the two are theorized to differ because of a symmetry-breaking mechanism.

So, if SUSY is true, for each Feynman diagram with an infinite fermion loop in the Higgs boson propagator, there is another diagram from the super-partners giving a contribution identical in magnitude but with opposite sign. The magnitude is the same because (from the unbroken perspective) the particles are identical; the sign is opposite because amplitudes receive a factor of -1 for each fermion loop within it due to the spin-statistics theorem [7]. Each higher-order diagram giving infinite contribution is thus canceled by its super-partner's diagram.

Thus SUSY offers a solution to the Higgs mass problem[4]. This gives some indication that it is "true," and that it is perhaps not only a theory on paper but exists in the physical world, and therefore warrants experimental tests. This is not its only motivation. Besides the theoretical allure of unifying two very different classes of particles (bosons and fermions), it is also well-motivated because it indirectly helps to elucidate one of the other problems in the standard model, that of gravity.

[4]Currently, it is the most popular solution to this problem, although popularity of an unverified theory can be viewed as meaningless. In some sense, though, the popularity of a theory is an indicator of how much the entire particle physics community considers the theory to be well-motivated. To the extent that the collective intelligence of physicists can be trusted, a popular theory can be seen as a good theory. While this figure of merit should probably not be completely dismissed, it is not always reliable—remember parity violation [8]. In the end, there is no substitute for experiment.

1.1.3 The Gravity Problem

Gravity is noticeably absent from the standard model. While across all energy scales currently probed standard model predictions are confirmed by experiments, at some short distance scale gravitational effects must become important, and a full theory that describes all fundamental interactions (electroweak, strong, and gravitational) is required to make predictions. A simple and often-used example is the collision of two particles with a center-of-mass energy equal to the Planck mass, 10^{19} GeV (I had first seen an example of this type in [9]). With this beam energy, the collision probes de Broglie wavelengths of roughly $\lambda/\pi \sim 10^{-35}$ meters.[5] But, an object with this mass has a Schwarzschild radius of roughly $r_s \sim 10^{-35}$ meters.[6] That is, the Planck scale is defined as the point at which quantum and gravitational scales become the same[7].

The Planck scale thus gives the scale at which gravitational effects must become important, and the scale at which experimental probes could best elucidate the full theory of the fundamental interactions. Using current particle acceleration technologies, we could make such a probe simply by scaling the size of

[5] Obtained via $E = h\nu = 2\pi\hbar c/\lambda$, where E is the beam energy.

[6] Obtained via $r_s = 2GM/c^2$, and using $M = E/c^2$.

[7] This point is found by an extrapolation with equations known to be valid at the scales that the current theories of quantum physics and general relativity are each known to be valid. Of course, this extrapolation could break down before the Planck scale is reached. For example, it has been suggested that the real Planck scale could be much lower than usual arguments suggest because of "compactified" extra dimensions [10].

current accelerators up by 15 orders of magnitude, from $O(1)$ km to $O(10^{15})$ km. Unfortunately the solar system could not accommodate an accelerator of this size (the solar system is 10^5 times to small), although our galaxy could (it's 10^3 times bigger than necessary). Clearly a radically different accelerating technology or a radically different experimental approach would be helpful[8].

Because of the absence of the experimental tools at appropriate scales, the full theory of the fundamental interactions that includes gravity remains unknown. The current most popular contender for this full theory is string theory [11]. While this theory is not developed enough to make testable predictions, nor are experiments currently able to probe the necessary distance scales, indirect verification can be sought through a search for SUSY, since most varieties of string theory require a boson-fermion symmetry to function. While a failure to discover SUSY would not necessarily rule it out, confirming it would likely shed light on the nature of string theory, and provide additional insight as to whether or not it has any bearing on the physical world. To put it in a more model-independent way that does not emphasize string theory, full theories that include gravity will likely be constrained by proof or disproof of SUSY at the electroweak scale.

[8] A new technology or approach is not necessary to probe the Planck scale, though, if the authors of [9] and [10] (and authors of references therein) are correct in theorizing the Planck mass is lower than usual arguments suggest.

We have thus seen that SUSY is a reasonably well-motivated theory that offers solutions to and helps elucidate some of the current outstanding problems in particle physics. There are other reasons to consider it well-motivated. It offers a natural dark matter candidate, and there is some indication it leads to gauge coupling unification at some high energy scale [6]. It therefore deserves experimental scrutiny. We now describe its possible experimental signatures, along with the experimental signatures expected for GUTs.

1.2 Experimental Signatures

We have seen some of the standard model's most glaring deficiencies and some well-motivated theories, GUTs and SUSY, that help address them. I search for the signatures of such theories, hoping to shed light on these problems in order to better understand the correct theory that offers solutions to these problems. But in order to search for these new theories, we must understand the experimental signatures that the theories predict.

1.2.1 Experimental Signatures for GUTs

As mentioned in Sec. 1.1.1, in most GUTs extra particles arise naturally. The nature of the new particles is not well-constrained; they could be additional

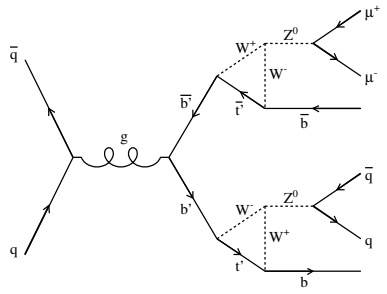

Figure 1.1: Possible dominant contribution to b' production and decay.

gauge bosons, additional fermions, perhaps grouped into another generation[9], or something else entirely. The possibility of an additional generation of quarks was discussed in [12]. As they discuss, if the down-type quark of the added generation (b') has a mass less than $m_t + m_W$, the decay $b' \to tW$ is kinematically suppressed, and the decay $b' \to cW$ is doubly Cabibbo suppressed. In this mass range, the decay channel $b' \to bZ$ would potentially be dominant, as shown in the Feynman diagram in Fig. 1.1. This would lead to a signature in which there were at least one Z in the event with many extra jets[10].

While the $b' \to bZ$ decay would be dominant, the weak coupling of the loop decay could lead to a potentially long-lived b'. In this scenario the b' might

[9] Although an additional generation of leptons with a light neutrino is constrained by LEP measurements of the Z width.

[10] In quantum chromodynamics (QCD), free quarks and gluons with non-zero $SU(3)$ charges do not last long, and instead hadronize into $SU(3)$ singlet states, showing up as a "jet" of particles in the detector. See [1].

decay at measurable distances displaced from the beam, leading to displaced Z boson decays. The $Z \to ee$ and $Z \to \mu\mu$ decay channels are easily vertexable and have low, well-understood backgrounds, making them ideal samples to study long-lived particles coupling to the Z boson. In addition, as there are absolutely no standard model processes that allow on-shell Z's to be produced at displaced vertices, this signature, if observed, would be a compelling sign of physics beyond the standard model.

1.2.2 Experimental Signatures for SUSY

While a key advantage of SUSY is its solution of some of the standard model's problems, a key drawback is its ability to evade experimental constraints. With its more than 100 additional free parameters [6], it can appear in many possible final states.

The number of final states is reduced somewhat by focusing on the lightest supersymmetric particle (LSP) of various SUSY scenarios. The LSP is significant because in many SUSY scenarios it is stable because of assumed R parity conservation. One therefore naively expects, in every event that contains a SUSY particle, a cascade of decays down to the stable LSP. Furthermore, in order to offer a natural dark matter candidate, the LSP is theorized to be charge-neutral.

Because it is stable, weakly-interacting, and charge neutral, it leaves no trace in the detector, causing many SUSY searches to focus on missing energy[11] [13].

The simplest charge neutral particle in SUSY (and therefore the simplest dark matter candidate) is the neutralino, a mass eigenstate consisting of a mixture of the neutral supersymmetric particles, the zino, photino, and higgsino. Depending on details of this mixture and the various sparticle masses, various decay channels to the LSP can dominate. The authors of [14] explored a SUGRA (supergravity) scenario in which the production and decay of the next-to-lightest supersymmetric particle (NLSP) to the Z boson and the LSP dominates. Because of the cascade decays, one expects additional activity in the event, possibly in the form of jets.

In addition, the authors of [15] explored a scenario in which the LSP was assumed to be a gravitino, leading to decays of neutralinos to the LSP and gauge and Higgs bosons. In this scenario, because of the extremely weak coupling to gravity, the lifetime of the NLSP was extremely long, leading to the possibility of gauge and Higgs boson production at measurable distances displaced from the beam. Displaced production of the photon, W, Z, and the Higgs would then be possible. The displaced photon channel has been explored by others [16]. Displaced vertices of the W boson would be difficult to measure, as the

[11] Or missing transverse energy ($\not\!\!E_T$) at hadron colliders, since there the center-of-mass frame not known.

dijet channels have large backgrounds, and vertexing the $\ell\nu$ channel is extremely difficult as the neutrino trajectory cannot be reconstructed with any precision. Finding displaced vertices of the Higgs, an undiscovered particle, is experimentally challenging, as there is little *a priori* knowledge of its decay channels and there are no control samples for calibration. But again, the ee and $\mu\mu$ channels of the Z boson are ideal places to look for long-lived particle decays.

1.2.3 My Focus

We have seen two types of theories, GUTs and SUSY, that offer solutions to the standard model's problems. Both of these models predict new particles coupling to Z bosons in various regions of their parameter space. In particular, both allow the possibility of long-lived parents of the Z, and for enhanced production of Z+jets. In this thesis, I describe my study of these final states, and our searches for anomalous behaviors in these channels that could not be explained by the standard model or detector effects.

Of course in the big picture, these channels, while well-motivated, are just one of many. Because the theory that lies beyond the standard model is unknown, all channels could be well-motivated by some theory. It therefore becomes necessary to look in all channels, which the many members of large high energy experimental collaborations indeed try to do. Although the effort of cataloging

and systematically checking each final state is sometimes not obviously apparent. Rather, which channels receive attention are governed by free market patterns, with the more promising channels (like the standard model Higgs final states) attracting more analyzers, while less promising channels (like, say an $e^+\mu^+\tau^+\gamma\not{E}_T$ final state) attracting few analyzers. Which channel to choose can become a bet on where one believes new physics is most likely to arise. The W and Z gauge bosons, with their large mass and key role in electroweak symmetry-breaking, are two final states that are potentially promising. Of these two, the Z boson's dielectron and dimuon final states are very experimentally clean, a large asset at a hadron collider. For these reasons, we (me, my advisor, and his group) have placed our bets on the $Z \to ee$ and $Z \to \mu\mu$ final states, wagering that our effort spent on these analyses has good odds of resulting in a discovery payoff.

Before I get into the details of the analyses, it is necessary to describe the two main pieces of (large) hardware necessary for these searches. They are the particle accelerator, the Tevatron, and the detector, the Collider Detector at Fermilab (CDF).

Chapter 2

Experimental Setup

2.1 The Tevatron

The Tevatron is a particle accelerator that provides collisions of protons with antiprotons. How the Tevatron accelerates these particles is extremely interesting, important, and will not be described here in any detail. It has been described by others in [17]. I provide a standard schematic of it in Fig. 2.1, and give a brief overview here.

It starts with neutral hydrogen gas (H_2), fed into an ion source that produces H^- by heating the gas to a plasma in the presence of electric and magnetic fields. These H^- ions are then accelerated to 200 MeV with a linear accelerator, and then passed through a foil, stripping off the electrons and leaving the protons,

H^+. These protons are sent through various accelerators, and some are diverted for antiproton production, and aimed at a target (currently made of a nickel alloy [18]). The protons in the beam interact with the protons in the target nuclei, making protons via the low-rate baryon-conserving $pp \rightarrow pppp\bar{p}$ reaction. Only $O(10)$ antiprotons are created from $O(10^6)$ protons on target. After a sufficient supply of antiprotons are made, protons and antiprotons are injected (with opposite directions) into the last accelerator in the chain, the Tevatron. The Tevatron does the final acceleration of the proton and antiprotons from 150 GeV to 980 GeV by ramping up its magnets in synchronization with its electric fields. The beams are then focused and collided at two interaction points, one at the DØ experiment, and another at the Collider Detector at Fermilab (CDF) experiment.

2.2 Accelerators in General

Without the collisions provided by the Tevatron, this thesis would not be possible. As alluded to in Chapter 1, high-energy collisions are the primary tool that particle physicists use to examine distance scales that have not yet been explored. For this type of endeavor, three things are absolutely necessary:

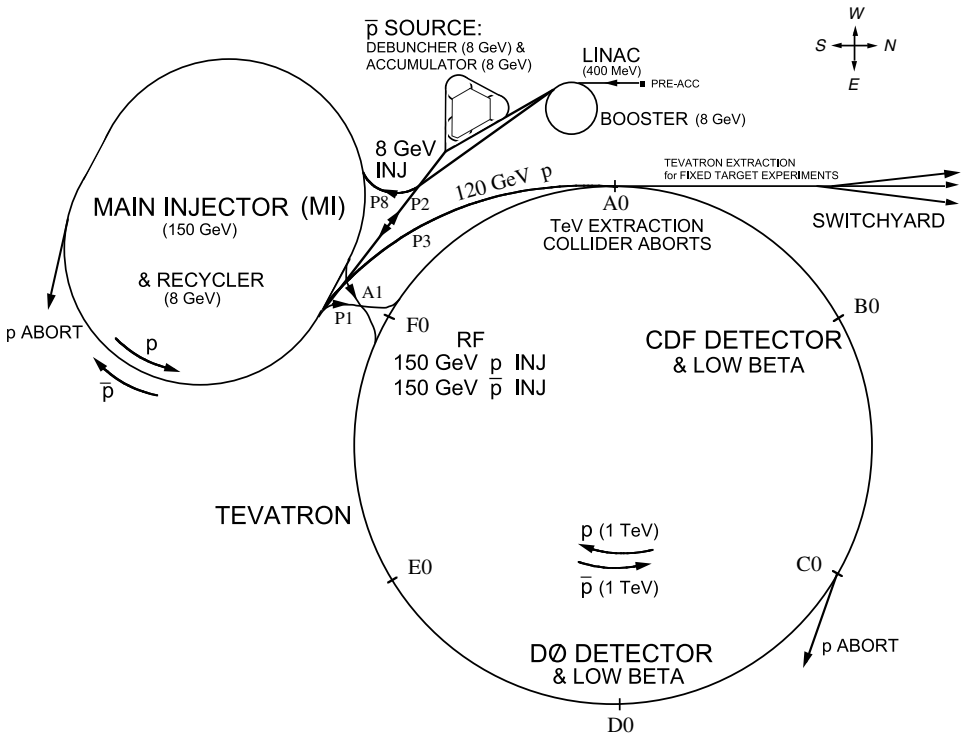

Figure 2.1: Schematic of the Tevatron as seen from above.

1. High energy collisions. (Where "high" means the energy scale at which you expect new physics. If you have no theoretical expectation, this can be taken to mean anything higher than what has already been explored.)

2. A lot of these collisions. That is, high luminosity. (High enough so that you can see the new physics, typically produced with low cross section).

3. A detector to see what happened during the collisions.

Most of the work done within the particle physics community is focused on requirement 3. Particle physicists build large, elaborate detectors that are able to observe the different types final states that can occur in the high-energy collisions. Requirements 1 and 2 are largely relegated to a completely different field, that of accelerator physics. While there may be good reason for this divergence, probably related to the complexity and disparity of the two subjects, requirements 1 and 2 are extremely important. That is, finding a way to more easily and more cheaply collide particles with higher energy and higher luminosities would have an enormous impact on particle physics. Because of its importance, and because of the lack of attention it receives by the particle physics community, I started a collaborative effort with some accelerator physicists, with our focus on requirement 1—higher energy. Our work is documented in [19, 20]; I will describe it briefly here.

2.3 New Acceleration Technology

The goal is to obtain extremely large electric fields for use in particle acceleration. Current accelerators, such as those at the Stanford Linear Accelerator Center (SLAC) [21], have average accelerating fields of approximately 10 MV/m. If this field were to be increased by a few orders of magnitude, to 10 GV/m, the $\sim$ 3000 meter SLAC beamline could be reduced in size to a mere 3 meters. Plasma wakefield acceleration (PWFA, described in [22]) has the potential to achieve fields of this size. In PWFA, a beam (either laser or particle) is shot through a plasma. This driving beam alters the spatial configuration of the plasma electrons, setting up a "wakefield," containing an electric field pointed along the beam direction with large-magnitude. This wakefield trails the beam with a velocity equal to the beam velocity. This field can be exploited, accelerating a second particle beam injected after the driving beam. In particular, there is a proposal for a linear collider "afterburner," in which a set of PWFAs is placed right before the interaction region of the two beams of a conventional linear accelerator/collider, with an approximate doubling of the beam energy as a goal.

Much of the previous work in PWFA has been in the regime in which the plasma nuclei ions are relatively stationary, with only the plasma electrons mov-

ing. Substantial nuclei ion motion can lead to time-varying transverse fields that cause the beam to defocus. In [19], we examined plasma densities in the afterburner scenario, using beam parameters likely for the next generation linear collider. In our simulations, we found that violent nuclei ion motion is likely, casting doubts on the feasibility of a linear collider afterburner. We pursued an approach to mitigate this problem.

One possible solution to the nuclei motion problem is to do away with the nuclei entirely. That is, rather than using a plasma to cause the wakefield, instead use a dielectric material to set up a wakefield. The potential of such an accelerator would be limited by the properties of the dielectric—above a certain accelerating field, the dielectric would not be able to sustain its internal electric field, resulting in breakdown. However, as there is little previous experimental work on beam wakefield generation in dielectrics, this maximum possible accelerating gradient is not known. We therefore performed an experiment to find this maximum field in a certain dielectric material, fused silica.

In the experiment, aluminum-coated fused silica capillary tubes (with relative permittivity $\epsilon \sim 3$) with length $\sim$ 1 cm, and inner radii 50 and 100 μm were used. An electron beam, provided by the SLAC Final Focus Test Beam (FFTB) was shot through the tube centers with energy 30 GeV, charge 3 nCoul, radius (σ_r) 10 μm, and length (σ_z) ranging from 20 to 100 μm. The radial electric field

on the inner surface of the dielectric is inversely proportional to the beam length σ_z. We therefore expect that as the beam length is decreased, the fields within the dielectric will increase, and breakdown may be observed below some beam length.

When running with longer beam lengths (100 μm), we observed visible wavelength light emission, believed to be some combination of Cherenkov radiation, transition radiation, and scintillation. As the beam length was decreased, we saw a drastic increase in the intensity of the light, consistent with what one would expect from plasma formation during breakdown. This breakdown occurred at beam lengths near 60 μm, corresponding to theoretically-calculated surface electric fields of 3-4 GV/m. From simulations, this is believed to correspond to a wake accelerating field of 1.5–2 GV/m. While these fields do not currently seem as promising as those of plasma wakefield acceleration, these measurements are preliminary. Further work is planned, with an immediate goal of independently measuring the field within the dielectric by measuring the properties of coherent Cherenkov radiation that it emits.

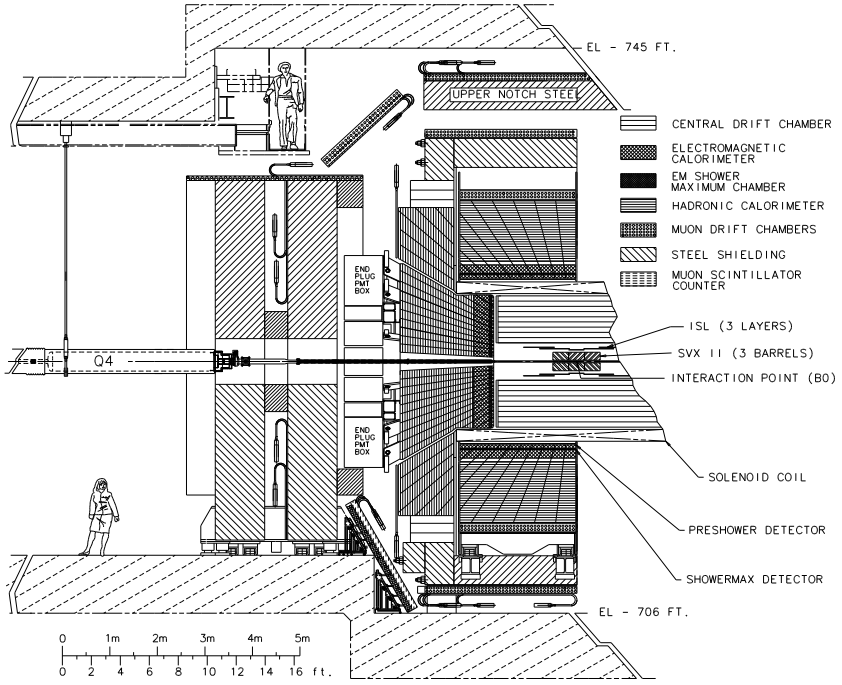

Figure 2.2: Schematic of the CDF detector.

2.4 The Detector

After that brief detour through the world of accelerator physics, let us get back to the thrust of the thesis: my work on the particle collisions produced by the Tevatron and detected by CDF. It will be necessary for the reader to have an understanding of the CDF II detector. I provide a standard schematic of it in Fig. 2.2. As usual, it has been described in detail by others [23]. I simply give a brief overview here.

I first must describe the coordinate system conventions. In the CDF coordinate system, the origin is the center of the detector, and the z axis is along beam direction, with positive defined as the proton beam direction. The x axis points radially outward from the Tevatron ring, leaving the y axis direction perpendicular to the earth surface with positive direction upward. Spherical coordinates are used where appropriate, in which θ is the polar angle (zero in the positive z direction), ϕ is the azimuthal angle (zero in the positive x direction), and the pseudorapidity η is defined by $\eta \equiv -\log[\tan(\theta/2)]$. At hadron colliders, transverse energies and momenta are usually the appropriate physical quantities, defined by $E_T \equiv E \sin\theta$ and $p_T \equiv p \sin\theta$ (where E is a particle's energy and p is the magnitude of a particle's momentum).

A tracking system is situated directly outside the beam pipe and measures the trajectories and momenta of charged particles. The innermost part of the tracking system is the silicon detector, providing position measurements on up to 8 layers of sensors in the radial region $1.3 < r < 28$ cm and the polar region $|\eta| \lesssim 2.5$. Outside of this detector lies the central outer tracker (COT), an open-cell drift chamber providing measurements on up to 96 layers in the radial region $40 < r < 137$ cm and the polar region $|\eta| \lesssim 1$. Directly outside of the COT a solenoid provides a 1.4 T magnetic field, allowing particle momenta to be obtained from the trajectory measurements in this known field.

Surrounding the tracking system, segmented electromagnetic (EM) and hadronic calorimeters measure particle energies. In the central region, the calorimeters are arranged in a projective barrel geometry and cover the polar region $|\eta| < 1.2$. In the forward region, the calorimeters are arranged in a projective "end-plug" geometry and cover the polar region $1.2 < |\eta| < 3.5$. Two sets of drift chambers, one directly outside the hadronic calorimeter and another outside additional steel shielding, measure minimum-ionizing muon trajectories in the region $|\eta| < 0.6$; another set of drift chambers similarly detects muons in the region $0.6 < |\eta| < 1$. Muon scintillators surround these drift chambers in the region $|\eta| < 1$ for trigger purposes. A luminosity measurement is provided by Cherenkov detectors in the region $3.7 < |\eta| < 4.7$ via a measurement of the average number of $p\bar{p}$ collisions per crossing [24].

Collision events of interest are selected for offline analysis using a three level trigger system, with each level accepting events for processing at the next level. At level 1, custom hardware enables fast decisions using rudimentary calorimeter and tracking information with a simple counting of reconstructed objects. At level 2, trigger processors enable decisions based on partial event reconstruction. At level 3, a computer farm running fast event reconstruction software makes the final decision on event storage.

2.4.1 Silicon

The above describes the major components of the CDF detector. Building and maintaining them all require a great deal of resources. I have worked on one of these components in particular, the silicon detector.

The first of my efforts was related to the portion closest to the beam, consisting of a layer of sensors called "layer 00" (L00), validating that it was working properly *in situ* during real collisions. First, I verified that L00 was indeed detecting particles that passed through it. To do so, using others machinery, I took tracks reconstructed from the COT and the outer silicon detectors, extrapolated them in to L00, and obtained the nearest hit. I found that L00 did indeed output hits with the expected charge and with high efficiency, verifying that each of its pieces were functioning properly and in unison—from the sensors themselves to the reconstruction software. I was able to debug some problems, such as differences between the detector layout expected by the reconstruction software and what actually existed. After this validation, I was able to do a global alignment, correcting for a global rotation and translation of L00 from the positions used in the reconstruction software.

The remainder of my efforts were concerned with the maintenance of the entire silicon detector. The detector and its components can fail for a number of reasons—regular use, beam incidents, human error and meddling, etc. It

is necessary to periodically verify that hits from charged particles are indeed being collected, read out, and recorded on each of the ∼750,000 channels. To do so, we check, in each module (called a "ladder") that the collected charge of hits on tracks matches the expected Landau distribution, and matches what was collected at previous times. If it does not, we examine the ladder further, checking if the problems are associated with specific portions of the ladder, or are associated with various pieces of the power supply or readout electronics, providing diagnoses and suggesting approaches to fixing the problems.

Finally, now that the theoretical and experimental background is described, let's finally jump into the main part of the thesis—the analyses I did on searches for new physics that couple to Z bosons.

Chapter 3

Selecting Z's

In order to search for new physics coupling to Z bosons, one must first be able to detect them. As Z bosons decay immediately (within $\sim 10^{-25}$ seconds), one must detect their decay products. The $Z \to ee$ and $Z \to \mu\mu$ decay channels are most easily observed, particularly at hadron colliders. This is true for two reasons.

First, both a single electron and a single muon are relatively easy to detect. In the electron case, energy in the electromagnetic calorimeter, absence of energy in the hadronic calorimeter, and an isolated matching track in the tracking system (in our case the COT) constitutes an electron detection. In the muon case, absence of significant energy in the electromagnetic and hadronic calorimeters,

an isolated well-measured matching track in the COT, and hits in the muon chambers constitutes a muon detection.

Second, at hadron colliders, the largest cross sections are due to QCD (quantum chromodynamics) processes, with quark and gluon final states forming jets after hadronization. These processes usually do not create isolated electrons or muons, and formation of electron or muon pairs is even rarer. Thus the $Z \to ee$ and $Z \to \mu\mu$ channels have low background at a hadron collider like the Tevatron.

These are the final states we use. As mentioned in Sec. 1.2.3, we use these final states for two analyses: a search for long-lived particles decaying to Z bosons, and a search for new particles coupling to Z+jet. The former analysis, done first, uses only the $Z \to \mu\mu$ decay channel, and uses less data (a integrated luminosity of 163 pb^{-1}). The latter analysis, done later, uses both $Z \to ee$ and $Z \to \mu\mu$ decay channels, and uses 1.08 fb^{-1} of $Z \to ee$ data and 1.04 fb^{-1} of $Z \to \mu\mu$ data. As the analyses were done at different times (with the understanding gained in the first analysis feeding in to the second analysis) and are rather experimentally different (the long-lived parent analysis has more emphasis on well-measured tracks) each analysis has its own specific selection. After describing the general strategy for triggering and selecting Z bosons, I

describe each of these selections separately in the individual chapters describing each analysis.

3.1 Overall Selection Strategy

The $Z \to ee$ and $Z \to \mu\mu$ candidate events are collected using single electron and muon triggers. The electron trigger requires at least one central electromagnetic energy cluster with $E_T > 18$ GeV and a matching track with $p_T > 9$ GeV/c. The muon trigger requires at least one central track with $p_T > 18$ GeV/c with matching hits in the muon drift chambers.

Z candidate events are selected offline by requiring at least one pair of electron or muon candidates both with $p_T > 20$ GeV/c and invariant mass in the range $81 < M_{\ell\ell} < 101$ GeV/c^2.[1] To increase efficiency, only one of the lepton pair has stringent identification requirements (the "tight" candidate), while on the other lepton the identification requirements are relaxed (the "loose" candidate).

"Loose" electron candidates consist of well-isolated EM calorimeter clusters with low energy in the hadronic calorimeter; in the central part of the detector ($|\eta| < 1.2$) well-measured tracks from the COT are required; in the forward

[1] I use the symbol "ℓ" to mean either an electron (e) or a muon (μ). While this symbol is chosen because it stands for "lepton," I do not intend for it to mean the third generation charged lepton τ, nor any of the neutrinos, as these particles are both very experimentally different.

parts of the detector ($|\eta| > 1.2$) no track is required, but the shower shape in the EM calorimeter is required to be consistent with that expected from electrons. "Tight" electron candidates have all the requirements of "loose" candidates, and are additionally required to be central ($|\eta| < 1.2$), to have a shower shape consistent with that expected from electrons, to have calorimeter position and energy measurements consistent with its matching track, and to have no nearby tracks consistent with that expected in electrons from photon conversions.

"Loose" muon candidates consist of well-measured tracks in the COT and well-isolated EM and hadronic calorimeter clusters with minimal energy deposits. "Tight" muon candidates have all the requirements of "loose" candidates, and are additionally required to have matching hits in the muon drift chambers.

All electron and muon pairs are required to be consistent with originating from the same z vertex, and to have timing information from the COT inconsistent with that expected for cosmic rays.

Chapter 4

Search for Long-Lived Parents of the Z Boson

We search for new long-lived particles that couple to the Z boson, as this would provide interesting evidence for physics beyond the standard model. As the Z is short lived, its $\mu\mu$ decay products originate at the point of its creation. Thus, any muon pair from a Z decay that is produced at a location outside the beam intersection (and cannot be explained by measurement mistakes) is evidence for a particle created at the beam, traveling a displaced location, and then decaying to a Z (and most likely something else). Therefore, in this search, after selecting $Z \to \mu\mu$ decays, we calculate the intersection of muons and see if any come from a vertex displaced from the beam. As electrons are more

susceptible to Bremsstrahlung, we do not add the $Z \to ee$ decay channel, as the backgrounds are quite different.

To find displaced dimuon vertices, we look for muon pairs with large L_{xy}, where L_{xy} is the distance in the transverse (xy) plane (z displacements are not well-measured) from the beam position to the track intersection (see Fig. 4.1). The calculation is done by analytically finding the intersection of the two muon tracks in the xy plane. We define the sign of L_{xy} from the angle θ in Fig. 4.1. Positive L_{xy} events are defined as those with the Z p_T in the direction of the displacement; negative L_{xy} events have the Z p_T opposite the direction of the displacement. More precisely, the sign of L_{xy} is defined as:

- If $\theta < 90°$, $L_{xy} > 0$
- Otherwise, $L_{xy} < 0$

The sign definition is made in this way because a signal is expected to appear with predominantly positive L_{xy}, while tracking mistakes are expected to be symmetric in positive and negative L_{xy}.

To validate the calculation of L_{xy}, we use $J/\psi \to \mu\mu$ events (triggered by requiring low p_T pairs of muons with a loose invariant mass cut). We show the invariant mass distribution of these events and their L_{xy} in Fig. 4.2. The L_{xy}

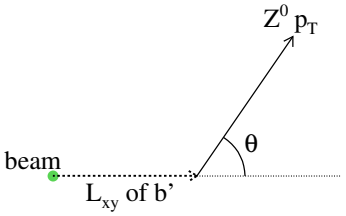

Figure 4.1: Illustration of L_{xy} and its sign definition.

distribution has a central core from prompt production, a positive tail from real displaced decays of B mesons, and a negative tail from tracking mistakes.

4.1 Selection

We select $Z \rightarrow \mu\mu$ events using the general strategy described in Chapter 3, with specific values listed in Table 4.1. This is similar to the muon selection of the Z+jet analysis, but additional track quality cuts are imposed, as the L_{xy} calculation requires well-measured tracks.

When the two tracks are nearly back-to-back, a small offset in the impact parameter of one track can lead to a large shift in L_{xy} as shown schematically

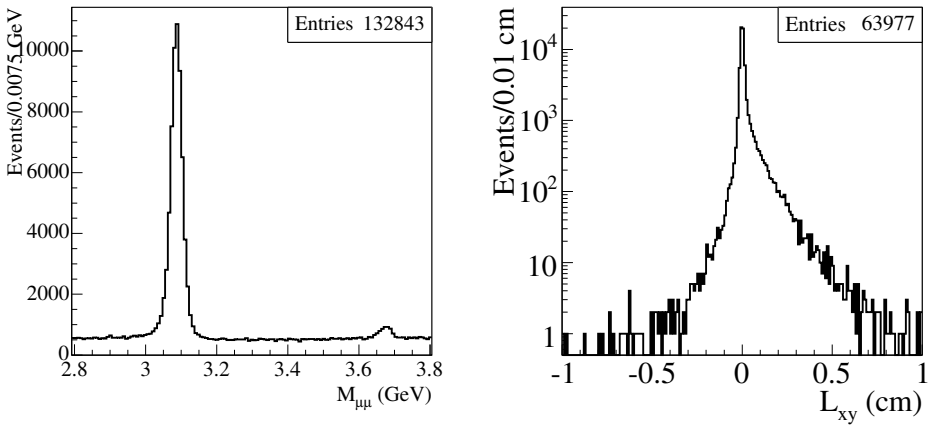

(a) (b)

Figure 4.2: Left: Distribution of invariant mass in J/ψ data. Right: L_{xy} distribution in J/ψ data, after applying an invariant mass cut of $3.02 < M_{\mu\mu} < 3.125$ GeV. Note the exponential on the positive side from decays of B mesons, and the negative tail from tracking mistakes.

p_T of each dimuon track	> 20 GeV
# of muons with $p_T > 20$ GeV	$= 2$
Invariant mass of dimuons	$81 < M_{\mu\mu} < 101$ GeV
Tracking Quality cuts:	
# of drift chamber hits	≥ 60
# of $r\phi$ silicon hits	≥ 3
Silicon χ^2/dof	< 8
(Track d_0 error)^2	$< (28\ \mu\text{m})^2$
(Track ϕ_0 error)^2	$< (0.2\ \text{deg})^2$
(Track $curv$ error)^2	$< 8 \times 10^{-12}\ \text{cm}^{-2}$
Δz of 2 muons at L_{xy} intersection	< 1.5 cm
$\Delta\phi_0$ of 2 muons	$2^\circ < \Delta\phi_0 < 175^\circ$
Δt_0 (for cosmic rejection)	< 3 ns
Muon ID Cuts, both legs:	
On both legs:	
E_{EM}	$< 2 + \max(0, 0.0115(p - 100))$ GeV
E_{Had}	$< 6 + \max(0, 0.0280(p - 100))$ GeV
Isolation Fraction	< 0.1
Muon Chamber Cuts, tight leg:	
CMU $\lvert\Delta\text{X}\rvert$	< 3.0 cm
CMP $\lvert\Delta\text{X}\rvert$	< 5.0 cm
CMX $\lvert\Delta\text{X}\rvert$	< 6.0 cm
Muon Chamber Cuts, loose leg:	No requirements
Signal Definition:	
With $p_T^Z > 30$ GeV cut	$L_{xy} > 0.03$ cm
Without a p_T^Z cut	$L_{xy} > 0.1$ cm

Table 4.1: Signal Selection

in Figure 4.3. To reject such events, we require $\Delta\phi < 175^\circ$ between the two muons. This rejects 99.8% of the large L_{xy} background but is very efficient for Zs produced with even a modest boost. Zs from the decay of a new particle would be boosted by the decay as well as any p_T of the parent.

High transverse momentum of the Z boson is a generic feature for such decays, so we additionally require $p_T^Z > 30$ GeV. However, we do not heavily optimize this cut to avoid undue model dependence. Furthermore, we perform the search both with and without the p_T^Z cut. That broadens the model independence and adds sensitivity at long lifetimes where the background is already low.

It is common in b-quark tagging to require large impact parameters for the tracks and a large significance of the measured L_{xy}. We do not apply such cuts in order to retain the full L_{xy} distribution as a measure of the L_{xy} resolution function.

We define, *a priori*, a minimum L_{xy} for the signal region based on the expected background calculated from standard model Z generated with PYTHIA [25] and processed with a full detector simulation [26]. The requirement is

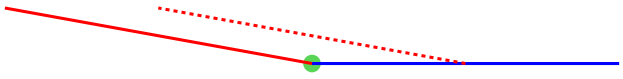

Figure 4.3: Since dimuons from Z's produced at rest are close to back-to-back, a small offset on one of the tracks (shown by the red, dashed line) produces a large shift in the measured L_{xy}.

$L_{xy} > 0.3$ mm which is tightened to $L_{xy} > 1.0$ mm in the case without a p_T^Z cut.

4.2 Backgrounds

The dominant background is from standard model Z bosons where mis-reconstruction of one of the muon tracks produces a large L_{xy}. We measure this background from Monte Carlo using the data in the central core of the L_{xy} distribution to tune the Monte Carlo resolution modeling. Three tuning methods are used and the differences are taken as a systematic uncertainty on the background prediction. We find backgrounds of 1.1 ± 0.8 events in the $p_T^Z > 30$ GeV case (and the looser $L_{xy} > 0.3$ mm cut) and 0.72 ± 0.27 events for the case without a p_T^Z cut (and the tighter $L_{xy} > 1.0$ mm cut).

The next largest background is from $b\bar{b}$ events where B hadrons, which have real displaced vertices, decay semileptonically to muons. We estimate this background by using Monte Carlo normalized to the number of large L_{xy} events in the data in an independent mass window of $50 < M_{\mu\mu} < 70$ GeV. Using the data for normalization naturally incorporates other muon sources such as decay-in-flight or punch-through. We find a background of 0.06 ± 0.06 events.

Cosmic rays have inherently large L_{xy}. We estimate the background they contribute from the number of events we remove with the cosmic rejection cuts together with the efficiencies of these cuts measured using a clean sample of cosmics. We calculate a background of 0.0004 ± 0.0001 events.

4.3 Acceptance $\times$ Efficiency

We measure the acceptance×efficiency for signal as a function of mass and lifetime using a combination of data and Monte Carlo. In the absence of a general model, we use the b' model to quantify the acceptance. We measure efficiencies for the muon identification and track selection using independently selected Z data and compare that to similar efficiencies measured from Z Monte Carlo. The ratio of the data and Monte Carlo efficiencies is used to scale a signal Monte Carlo calculation of acceptance×efficiency. This models the dependence of the efficiency on mass and lifetime using the Monte Carlo but normalizes that to the data.

We measure and apply the trigger efficiency using standard model Z candidates from data in which one leg is independently triggered. The tracking requirement in the trigger is not expected to be efficient for particles with very large impact parameter. We model this by removing events in which both muons

have impact parameters outside the acceptance of the track trigger. The remaining lifetime dependence of the acceptance e.g., tracking pattern recognition dependence on impact parameter, is taken from the Monte Carlo.

The acceptance×efficiency is shown as a function of lifetime and mass in Figure 4.4.

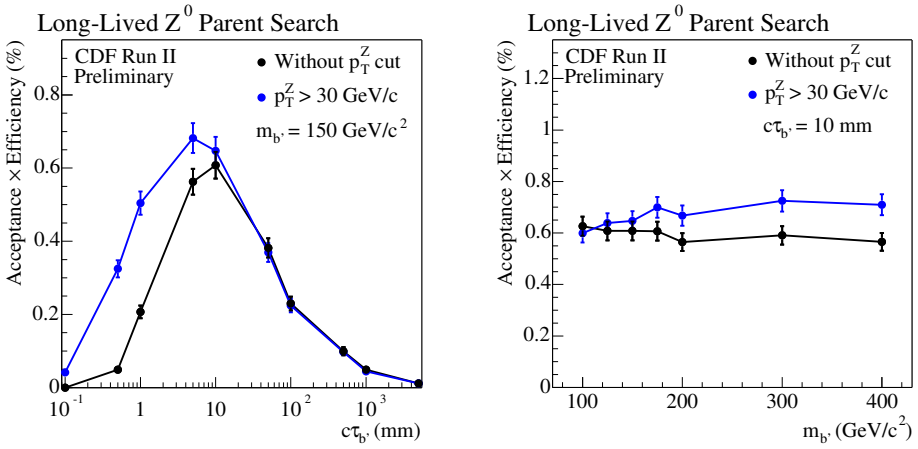

(a) (b)

Figure 4.4: Left: Acceptance×Efficiency versus b' lifetime for $m_{b'} = 150$ GeV. Right: Acceptance×Efficiency versus $m_{b'}$ for a lifetime of $c\tau_{b'} = 10$ mm. These include a factor from the branching ratio of $Z \to \mu\mu$.

Uncertainties on the efficiencies arise from the statistical precision with which they can be measured in the data and from systematic uncertainties in the Monte Carlo modeling. The modeling is found to be robust except for the silicon

χ^2/dof which is sensitive to variations in the other cuts. We assign an additional systematic uncertainty for this equal to its variation of 7.3%. We also include a systematic uncertainty of 0.9% due to uncertainty on the L_{xy} resolution based on the variations found in the background estimate described above.

The systematic uncertainties on acceptance arise from incomplete knowledge of initial and final state radiation (ISR/FSR) and parton distribution functions (PDF). We estimate the ISR/FSR uncertainty by suppressing each separately in PYTHIA. We use uncertainties equal to half of the change in each case. This is done at a few extreme mass and lifetime points and the maximum uncertainty found, 11.2%, is then used for all mass and lifetime values. The PDF uncertainty is calculated by re-weighting Monte Carlo events according to variations in 20 independent sets of CTEQ PDF parameters [27]. The resulting change in acceptance×efficiency, 2.0%, is used as an uncertainty.

4.4 Results

We plot the L_{xy} distribution of all selected events in Figure 4.5. We observe three events with $p_T^Z > 30$ GeV in the signal region of $L_{xy} > 0.03$ cm and two events in the signal region of $L_{xy} > 0.1$ cm without a p_T^Z requirement. In both cases, we see no events in the negative L_{xy} control regions.

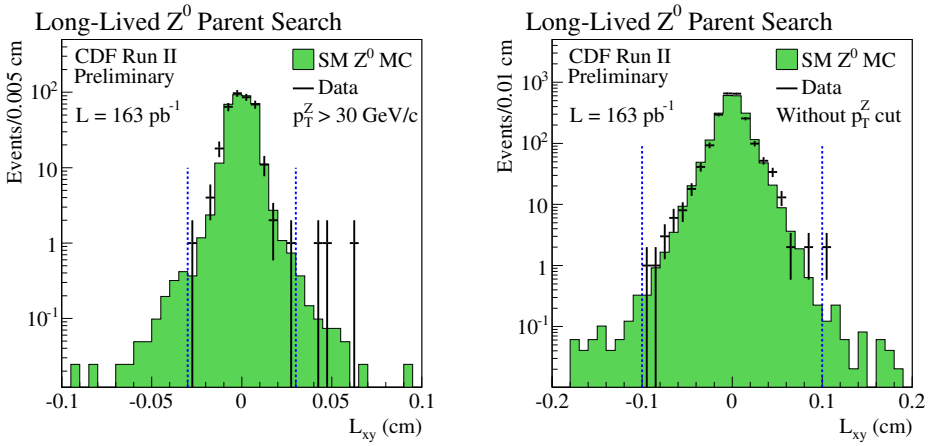

(a) (b)

Figure 4.5: L_{xy} distributions in data (points) and standard model Monte Carlo (green). Left: With $p_T^Z > 30$ GeV. Right: Without. The dashed lines indicate the signal and control regions.

The number of observed events is consistent with the background expectation, and *a posteriori* inspection of the events shows them to be consistent with mis-reconstruction as expected for background. A sample event is shown in Figure 4.6.

4.4.1 Limit

We calculate limits using the b' model for the acceptance×efficiency. The cross section limits are plotted as a function of lifetime and mass in Figure 4.7

along with the LO theoretical cross section calculated using PYTHIA. The resulting range of mass and lifetime excluded by this result is plotted in Figure 4.8.

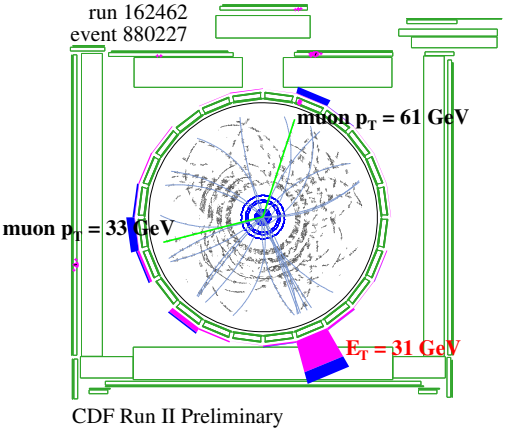

(a)

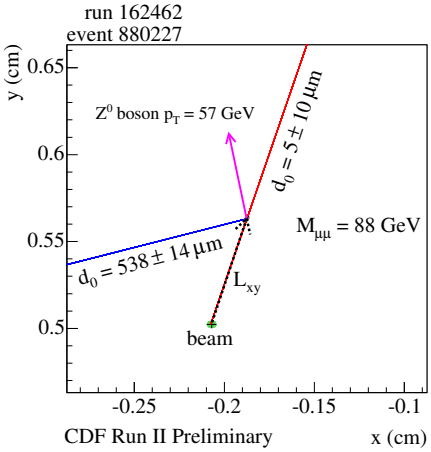

(b)

Figure 4.6: Sample event display. Top: A full xy view of the event showing the $Z \to \mu^+\mu^-$ recoiling against a jet with $E_T \approx 30$ GeV. Bottom: An enlarged view of the muon trajectories near the beam position. One of the tracks is consistent with the beam. The other is offset, most likely due to mis-reconstruction.

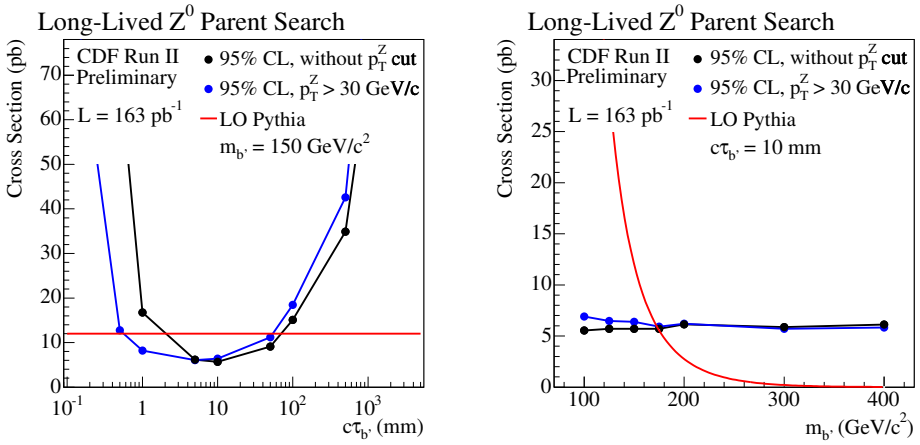

(a) (b)

Figure 4.7: Left: Cross section limits as a function of lifetime for $m'_b = 150$ GeV/c^2. Right: Cross section limits as a function of mass for a lifetime of $c\tau'_b = 10$ mm. The $b'\bar{b}'$ cross-section from PYTHIA is compared, assuming $BR(b' \to bZ) = 100\%$.

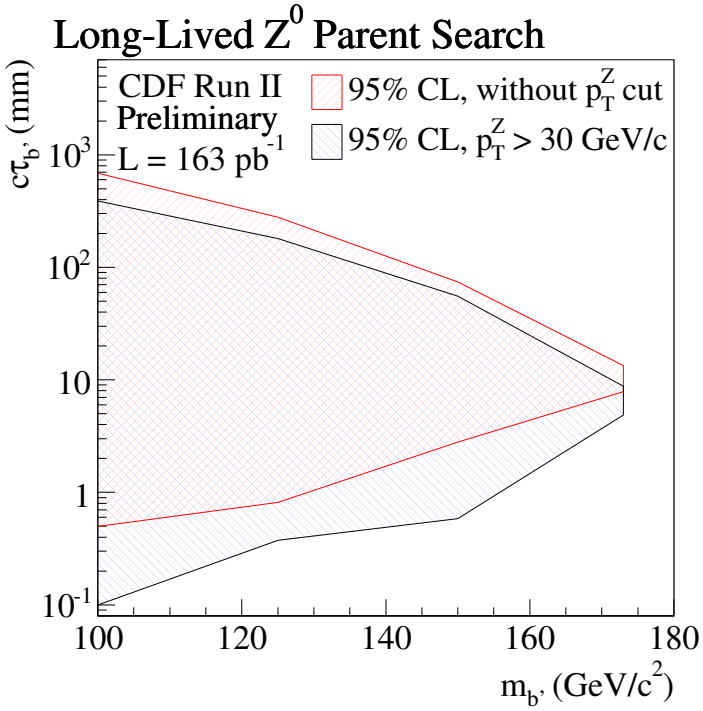

Figure 4.8: Lifetime vs. mass exclusion region in the b' model.

Chapter 5

Search for New Particles that Couple to Z+jet

We search for new particles that give rise to final states with a Z boson and additional jets. As described in Chapter 1, such a channel is well-motivated, with many beyond-the-standard-model theories predicting such final states [12, 14, 28, 29, 30]. We wish to discover or rule out these types of models, while maintaining model independence in the search. That is, while these theories offer guidance about the possible characteristics of physics beyond the standard model, they do not necessarily correspond to what actually exists in nature, and so we do not tailor the analysis to specific models.

We focus on final states in which there are at least 3 jets, each with at least 30 GeV of E_T. This choice was motivated by studying the optimal kinematic selection of a specific model, the b' model. While the selection was chosen as the optimal set of kinematic cuts using this model as a signal, this analysis constrains all models with Z+3 jet final states.

The dominant background of this final state is from standard model Z+jet production. Estimation of this type of background, with large numbers of high E_T jets, is not easy, as it contains non-negligible contributions from higher-order hard-scattering matrix elements in combination with soft non-perturbative QCD processes. Previous attempts of determining this type of background [31] have focused on calculating it from phenomenological first principles with the aid of Monte Carlo simulations. While calculation from first principles is appealing, because of its difficult nature, doing so requires careful validation with data. We develop a different approach, one that uses the data as more than a validation tool, and uses it alone for the background estimation.

5.1 Z Selection

We select $Z \to ee$ and $Z \to \mu\mu$ events using the general strategy described in Chapter 3. The specific muon cuts are listed in Table 5.1; the specific electron cuts are listed in Table 5.2.

Muon ID Cuts, both legs:	
p_T of each muon	> 20 GeV
E_{EM}	$< 2 + \max(0, 0.0115 \times (p - 100))$ GeV
E_{Had}	$< 6 + \max(0, 0.0280 \times (p - 100))$ GeV
Isolation Fraction	< 0.1
z_0	< 60 cm
# axial SL w/ ≥ 5 hits	≥ 3
# stereo SL w/ ≥ 5 hits	≥ 2
Impact parameter	$d_0^{Si} < 0.02$ cm or $d_0^{COT} < 0.2$ cm
Muon ID Cuts, tight leg:	
CMUP muons	$dX_{\rm CMU} < 3.0$ cm and $dX_{\rm CMP} < 5.0$ cm
CMX muons	$dX_{\rm CMX} < 6.0$ cm (CMX)
Muon ID Cuts, loose leg:	
	No stub requirements
Muon Pair Requirements:	
Invariant mass of muon pair	$81 < M_{\mu\mu} < 101$ GeV
Δz_0 of muon pair	< 1.5 cm
$\Delta\phi_0$ of muon pair	$\Delta\phi_0 > 5^\circ$
Δt_0^{COT}	< 3 ns

Table 5.1: Muon ID cuts.

Jets are clustered using the "MIDPOINT" clustering algorithm [32] with an η-ϕ cone size of 0.4 radians. Corrections are applied to extrapolate the jet energies back to the parton level using a generic jet response [33]. To remove

All Loose Electrons:	
E_T of each electron	> 20 GeV
Isolation Fraction	< 0.1
Loose Central Electrons:	
Had/EM	$\leq 0.05 + 0.00045 \times E$
# axial SL w/ ≥ 5 hits	≥ 3
# stereo SL w/ ≥ 5 hits	≥ 2
Track p_T	> 10 GeV
Track z_0	< 60 cm
Conversion flag	Conversion $! = 1$
Loose Plug Electrons:	
Had/EM	≤ 0.05
z_0 (if there is an associated track)	< 60 cm
PEM3x3FitTow	$! = 0$
PEM χ^2	≤ 10
PES 5x9 u & v	≥ 0.65
Tight Electrons:	
Central electrons only	$\eta < 1$
LshrTrk	≤ 0.2
E/p	≤ 2.0 or $p_T > 50$ GeV
CES ΔZ	≤ 3.0 cm
CES ΔX	$-3 \leq q \times \Delta X \leq 1.5$
CES Strip χ^2	≤ 10
Electron Pair Requirements:	
Invariant mass of Electron pair	$81 < M_{ee} < 101$ GeV
Δz_0 of Electron pair (if both have tracks)	< 1.5 cm
$\Delta\phi_0$ of Electron pair	$\Delta\phi_0 > 5^\circ$
Δt_0^{COT} (if both have tracks)	< 3 ns

Table 5.2: Electron ID cuts.

portions of the calorimeter more susceptible to jets from the underlying event and mis-reconstructions from beam remnants, we require all jets to have $|\eta| < 2$. Because, at CDF, real electrons get reconstructed as jets nearly 100% of the

time, we require that jets are well-separated in angle from an electron candidate by imposing $\Delta R(\text{jet} - e) > 0.4$ radians. To be consistent, we apply the same requirement in the muon channel.

5.1.1 Z Yield

For cross section measurements or limits on a given process, it is necessary to estimate the acceptance and efficiency to reconstruct events from that process. We calculate both the acceptance and efficiency using Monte Carlo events. However, as the efficiency to reconstruct leptons is not well-modeled by the Monte Carlo simulation, we measure these efficiencies in $Z \to \ell\ell$ data, and scale the Monte Carlo efficiencies to match that observed in data. With this approach, the dependence of the efficiency on various quantities is modeled with Monte Carlo and is normalized to the data. However, we have also checked that the Monte Carlo dependence of the efficiency on N_{jet}^{30} (the most important variable in this analysis) is consistent with that measured in the data.

To validate the selection, acceptance, and efficiency, we compare the $Z \to \ell\ell$ Monte Carlo simulations to the data. In Fig. 5.1, we show the distribution of $M_{\mu\mu}$ and M_{ee} in data and Monte Carlo simulation. The Monte Carlo events are scaled to the expected number of events, given the theoretical cross section of

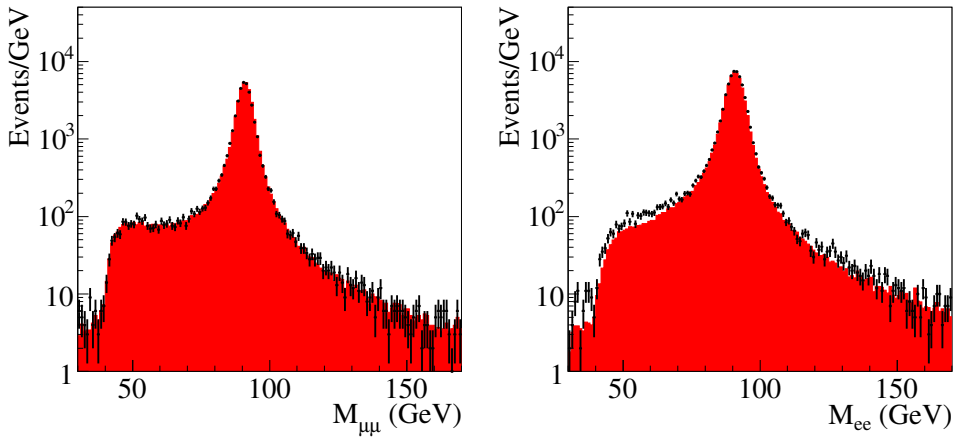

(a) (b)

Figure 5.1: Left: $M_{\mu\mu}$ measured in $Z \rightarrow \mu\mu$ data compared to Monte Carlo simulations. Right: M_{ee} measured in $Z \rightarrow ee$ data compared to Monte Carlo simulations.

250 pb[1]. In the muon case, the Monte Carlo agrees with the data quite well. In the electron case, there is still reasonable agreement, but there is a slight excess of the data above the Monte Carlo expectation. However, in this cross-check, we have not accounted for the presence of background. Since the background from dijet events is higher in the ee channel than in the $\mu\mu$ channel, an excess in the ee channel is not unexpected.

[1]This is the cross section of $p\bar{p} \rightarrow Z \rightarrow \ell\ell$ in the invariant mass region $66 < M_Z < 116$ GeV.

We can reverse this cross-check, and instead calculate the cross section of $Z \to \ell\ell$ in each channel. We do this as a function of run number (i.e. time) using the acceptance and efficiencies measured in Monte Carlo and corrected with data. At CDF, the muon chambers were not all operational for the entire range of data used, and were instead turned on in a piecemeal fashion. We therefore calculate the acceptance×efficiency in Monte Carlo for each of the different detector configurations separately, and find:

Run period			$A \times \epsilon$ (%)
	run	< 150144	10.86 ± 0.07
$150145 \leq$	run	< 154448	14.44 ± 0.06
$154449 \leq$	run	< 186597	14.41 ± 0.02
$186598 \leq$	run		15.11 ± 0.03

In the *ee* channel, the entire detector was operational for the full run range. The acceptance×efficiency from Monte Carlo for this detector configuration is $21.08 \pm 0.03\%$. We correct these using the efficiency measured in data and show the cross section vs. run number in Fig. 5.2.

In the muon case, the cross section is close to the expected cross section; in the electron case, the cross section is slightly (3%) high from the larger dijet background. In both cases, the cross section dependence on the run number is inconsistent with a flat function, although there are no pathological trends. This is likely due to luminosity-dependent (and therefore time-dependent) effects on the efficiencies and backgrounds that are not modeled by the Monte Carlo

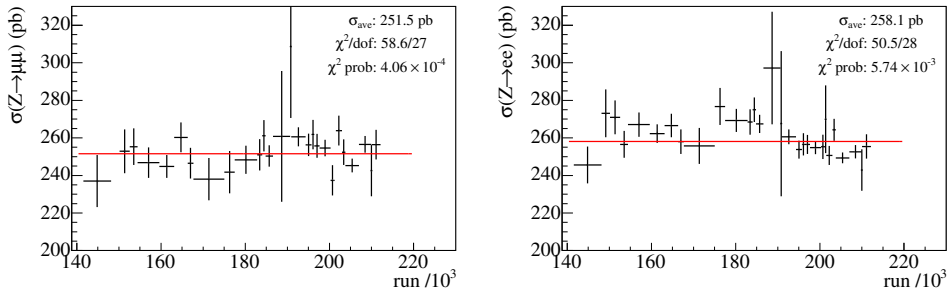

(a) (b)

Figure 5.2: Left: Measured cross section of $Z \to \mu\mu$ vs. run. Right: Measured cross section of $Z \to ee$ vs. run.

simulations. Because these effects are unmodeled, we measure them in data. The efficiencies, when measured in data over the entire run range, yield the correct average efficiency for that run range. Our data-based method of measuring the background, presented below, naturally takes into account these time-varying effects.

5.2 Kinematic Selection

As we expect new signals with large numbers of high E_T jets, we use the following discriminators to separate these from backgrounds:

$$\begin{aligned} N_{\text{jet}}^{X} &\equiv \text{Number of jets in the event with } E_T > X \text{ GeV} \\ J_T^{X} &\equiv \text{Scalar sum of } E_T \text{ of jets in the event with } E_T > X \text{ GeV} \end{aligned}$$

The thresholds X as well as the cut values on these variables are determined by optimization[2]. In the optimization we use the figure of merit $S/(1.5+\sqrt{B})$ (where S is the expected number of signal events and B is the expected number of background events) to quantify the sensitivity as a compromise between best discovery and best limit potential[3]. In the low background region ($B \ll 1$), maximizing this figure of merit is equivalent to maximizing the signal efficiency. In the high background region ($B \gg 1$), this figure of merit has the same behavior as $S/\sqrt{B}$. For the optimization study, we use $p\bar{p} \rightarrow b'\bar{b}'$ Monte Carlo simulations with a range of masses as the signal S. We use standard model Z Monte Carlo for the background B, generated with PYTHIA.

In order to be sensitive to a range of masses, we must take into account the generic behavior of new signals: as mass increases the cross section decreases while the transverse energy spectra become harder. Therefore, to be optimally sensitive to higher mass signals, we cut at larger values of $N_{\rm jet}$ and J_T thus removing more of the background to give sensitivity to the lower cross sections.

[2]In this section, it is useful to make a distinction between a "threshold" and a "cut." We define a "threshold" as a requirement on a jet E_T; we define a cut as a requirement on a variable made from individual jets. So, in the equation $N_{\rm jet}^{30} \geq 3$, we say that we have a 30 GeV threshold on the jet E_T, and we have a cut of at least 3 jets.

[3]The full sensitivity figure of merit obtained from Eq. (8) of [34] is more complicated than that used here. The one used here, $S/(1.5+\sqrt{B})$, is a reduced formula for the full figure of merit, in the case where the significance of discovery and the limit confidence level (both optimized for with this figure of merit) correspond to 3σ probabilities, and where the number signal and background events can be described by Gaussian (as opposed to Poisson) distributions.

For the sake of simplicity, we desire that our selection only changes gradually with mass and uses the same E_T threshold on all jets. To confirm that this desire for simplicity does not considerably reduce the search sensitivity, and to understand what cut values and thresholds to use, we first establish a "target" selection. The "target" selection is defined as the selection with the highest sensitivity when placing cuts on the individual jet E_T's and J_T. This is found by scanning through all possible cuts on J_T^{10} (that is, J_T is calculated with a 10 GeV threshold on the jets) and all possible E_T thresholds for up to 4 jets (ordered by E_T), and finding the point with the optimal sensitivity. In this scan, step sizes of 10 GeV are used for the jet E_T thresholds, and a step size of 50 GeV is used for J_T^{10}. This scan is done independently for b' masses in the range $100 \leq m_{b'} \leq 350$ GeV/c^2 with a step size of 50 GeV/c^2.

The optimal points found by this scan for a b' mass of 150 GeV/c^2 are shown in column 2 of Table 5.3. These cut values give the best possible sensitivity at this mass point when placing cuts on the individual jet E_T's and J_T^{10}. Again, we wish to choose a simple selection that gradually changes as a function of mass, and use the target sensitivities at all mass points for comparison. Based on the optimal target points for b' masses in the range $100 \leq m_{b'} \leq 350$ GeV/c^2, we choose the simpler requirements of $N_{\text{jet}}^{30} \geq 3$ and $J_T^{10} > m_{b'}c^2$. We compare the

Variable	Values from scan	Values of simple selection
$E_T^{\text{jet }1}$ thresh.:	50	30
$E_T^{\text{jet }2}$ thresh.:	30	30
$E_T^{\text{jet }3}$ thresh.:	30	30
$E_T^{\text{jet }4}$ thresh.:	20	0
J_T^{10} cut:	0	150
N_{sig}:	48.5	75.5
N_{bkg}:	2.60	13.8
$S/(1.5+\sqrt{B})$:	15.6	14.5

Table 5.3: Optimal point compared with the simple selection of $N_{jet}^{30} \geq 3$ and $J_T^{10} > 150$, for the $m_{b'} = 150$ GeV/c^2 mass point. Here, N_{sig} is the number of signal events expected in 1fb^{-1} after the given selection using b' Monte Carlo simulations. N_{bkg} is the number of background events expected in 1fb^{-1} after the given selection using standard model Z Monte Carlo simulations. In this optimization study, 2.7×10^5 standard model Z events were used; 1500 signal events were used (both counted before jet selection).

sensitivity of the simple requirements to the target sensitivity in column 3 of Table 5.3 for the 150 GeV/c^2 mass point.

From the table it is apparent that, for $m_{b'} = 150$ GeV/c^2, the sensitivity of the simple cuts is only negligibly less than the target sensitivity. We find the same to be true for all mass points studied, except for the $m_{b'} = 100$ GeV/c^2 mass point. In that case, however, the sensitivity of the simple cuts is still adequate

because of the larger cross sections for lower mass particles[4]. In addition, low masses near 100 GeV/c^2 are less interesting as they are already more tightly excluded [35]. Thus, we conclude that the simpler selection of $N_{\text{jet}}^{30} \geq 3$ and $J_T^{10} > m_{b'}c^2$ is nearly optimal for the mass range in which we are interested.

In the above, J_T was calculated using a 10 GeV E_T threshold on the jets. For the purposes of the background estimation, it is simpler to use the same E_T threshold on J_T as one uses on the N_{jet} variable. Therefore, we choose to use a 30 GeV threshold when calculating J_T. This was found to give a small decrease in sensitivity in the b' model with the benefit of a gain in simplicity.

The kinematic jet selection was found to be optimal when using the fourth generation model as the signal. When optimizing using the figure of merit $S/(1.5 + \sqrt{B})$, the optimal point is independent of the normalization of the signal. That is, any model with a different cross section but the same kinematic distributions will give the same optimal point. In addition, the shape of the kinematic distributions are mostly determined by the b' mass. We therefore expect that this selection is nearly optimal for all models with heavy particles produced in pairs and decaying to Z+jet. In general, this selection is sensitive

[4]For the $m_{b'} = 100$ GeV/c^2 mass point, the target selection has a signal of 450 on a background of 229, giving a figure of merit $S/(1.5+\sqrt{B}) = 27$. With the simple cuts, there is a signal of 64 on a background of 20, giving a figure of merit $S/(1.5+\sqrt{B}) = 11$. While the sensitivity figure of merit is smaller, a signal of 64 on a background of 20 is still adequate for a discovery.

to any model with high E_T jets in the final state. It may not be optimal for an arbitrary model, but designing a simple selection that is optimal for the entire class of Z+high E_T jet models is not possible.

In this optimization, we assumed new signals with final states consisting of a Z boson and many high E_T jets. Of course, some assumption about signal characteristics must be made in order to understand how to separate signal from background. These assumptions will naturally reduce the model independence of the search. There is a trade-off between the specificity of these assumptions and the sensitivity to a particular model. For example, in nearly all new physics models with Z boson final states, the transverse momentum of the Z is higher than that of the standard model Z. This is true because, in these models, the Z is usually a decay product of a massive particle. One would conclude that the Z transverse momentum is a very model-independent variable, and therefore well-motivated. However, we find, in the b' model sensitivity study, that the jet kinematic requirements have much higher sensitivity than the Z transverse momentum. The cost of this sensitivity is a loss of generality: with this assumption we are no longer sensitive to Z final states without high E_T jets. The sensitivity of the b' model can be further enhanced by requiring b jets using displaced vertices (because of the $b' \to bZ$ decay), again with a cost to generality. In our analysis, as a compromise between model independence and

sensitivity, we choose to only require additional jets in the event, without vertex tagging.

To summarize, after selecting $Z \to ee$ and $Z \to \mu\mu$ events, the kinematic selection is:

- $N_{\text{jet}}^{30} \geq 3$, and
- $J_T^{30} > m_{b'}c^2$.

That is, we select Z events with $N_{\text{jet}}^{30} \geq 3$, and scan the J_T^{30} distribution searching for an excess. We scan in step sizes of 50 GeV.

5.3 Backgrounds

In the signal region described above, there are potential backgrounds from the following sources:

- Single-Z production in conjunction with jets,
- Multi-jet events, where two jets fake leptons,
- Cosmic rays coincident with multi-jet events,
- WZ+jets, where the W decays to jets,
- ZZ+jets, where one of the Z's decays to jets,

- WW+jets, where both W's decay to leptons, and
- $t\bar{t}$+jets, where both W's decay to leptons.

The dominant background is from standard model single-Z production in conjunction with jets. Since beyond leading-log order diagrams make potentially large contributions to events with $N_{\rm jet}^{30} \geq 3$, calculation of this background from theoretical first principles is extremely difficult, and therefore would require careful validation with data. Rather than using data as merely a validation tool we take a different approach, and instead measure the background directly from data, and with data alone. We devote the following section to describing this prediction technique for the dominant background from Z+jet. The remaining backgrounds are then estimated later in Sec. 5.5.

5.4 Data-Based Z+jet Background Prediction Technique

Given the above selection, there are two tasks: we must predict the total number of background events with $N_{\rm jet}^{30} \geq 3$, and we must predict the shape of the J_T^{30} distribution after this cut. When combined, these two components give the full normalized J_T^{30} distribution prediction. The background for events with

$N_{\text{jet}}^{30} \geq 3$ and any J_T^{30} cut can be obtained from this distribution. I describe the method for predicting each of the two components separately in the following two sections.

In each of the prediction methods, we rely on fits to various jet E_T distributions. A parameterization that describes the shapes of these jet E_T distributions is therefore required. The parameterization used is:

$$f(E_T) = p_0 \frac{e^{-E_T/p_1}}{(E_T)^{p_2}}, \tag{5.1}$$

where the p_i are fitted parameters. This parameterization was motivated by observations in Monte Carlo simulations, control regions of data, and phenomenological studies that: at low E_T, the jet E_T shape follows a power law function; at high E_T, it follows an exponential decay function. The above parameterization satisfies these limiting behaviors. With the above convention, the parameter p_1 has dimensions of energy, the parameter p_2 is dimensionless, and both parameters are positive. Further discussion and motivation for this parameterization is provided in Appendix A.

5.4.1 Number of Events with $N_{\text{jet}}^{30} \geq 3$

In order to predict the total number of events with $N_{\text{jet}}^{30} \geq 3$, we use the jet E_T distributions in the $N_{\text{jet}}^{30} \leq 2$ control regions. Since jets are counted above an E_T

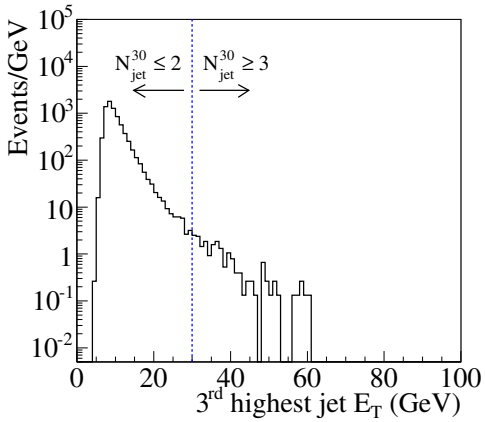

Figure 5.3: E_T distribution of the third highest E_T jet in standard model $Z \to \mu\mu$ Monte Carlo events. Events with $N_{\text{jet}}^{30} \leq 2$ have $E_T < 30$ GeV; events with $N_{\text{jet}}^{30} \geq 3$ have $E_T > 30$ GeV.

threshold (in this case 30 GeV), the N_{jet} distribution is completely determined from the jet E_T distributions. To illustrate this, and to merely describe the method, we use standard model $Z \to \mu\mu$ Monte Carlo events, generated with PYTHIA. After validation with control samples, the method is applied to the Z data.

In Fig. 5.3, we plot the E_T distribution of the third highest jet. By construction, a cut on $N_{\text{jet}}^{30} \leq 2$ separates this distribution into two regions. We can fit to this distribution in the $E_T < 30$ GeV region and extrapolate to the $E_T > 30$ GeV region to get the expected number of background events with $N_{\text{jet}}^{30} \geq 3$.

We fit the parameterization from Eq. (5.1) to the jet E_T distribution of Fig. 5.3, and show the results in Fig. 5.4[5]. The fit matches well the broad features of the distribution above 30 GeV. The number of events with $N_{\rm jet}^{30} \geq 3$ is then predicted by integrating the fitted distribution from 30 GeV to infinity. The fit prediction obtained with this method (with its uncertainty from fit parameter error propagation described in Sec. 5.4.3) is 116^{+10}_{-13} events (with the number of generated Monte Carlo events having an equivalent luminosity of 7 fb^{-1}).

The number of events in the Monte Carlo simulation is 152 events. In this case, the extrapolation predicts the background to within $31 \pm 16\%$. We will evaluate further the level of consistency in the validation studies with data in Sec. 5.4.4.

This method, using the jet E_T distributions to predict integrals of the $N_{\rm jet}$ distribution, can clearly be extended to other analyses as well. For illustration purposes only I describe other examples here, still using standard model $Z \rightarrow \mu\mu$ Monte Carlo simulation. Consider predicting the total number of events with $N_{\rm jet}^{80} \geq 1$ (that is, we require at least one jet with an E_T threshold of 80 GeV). In this case, a fit to the highest E_T jet distribution below 80 GeV can be extrapolated to above that threshold, as in Fig. 5.5. (Note that the highest

[5]We use unbinned likelihood-maximization fits. In practice, rather than maximizing the likelihood L, the quantity $-\log L$ is minimized. When comparing unbinned fits with binned histograms, we place the x-value of each bin at the average of the entries in that bin.

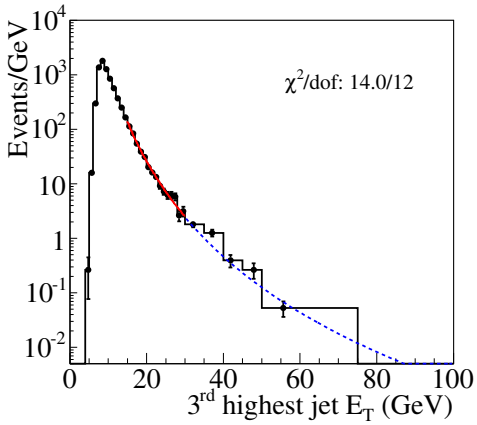

Figure 5.4: E_T distribution of the third highest E_T jet in standard model $Z \to \mu\mu$ Monte Carlo events. The distribution is fit to Eq. (5.1) in the range $15 < E_T < 30$ GeV, and extrapolated to the $E_T > 30$ GeV region.

E_T distribution in this figure is harder than the third highest E_T jet distribution, as one expects when ordering the jets by E_T). It is clear that the extrapolation describes the distribution reasonably well.

If we instead wish to predict the number of events with $N_{\text{jet}}^{40} \geq 1$, we must fit the same E_T distribution below 40 GeV and extrapolate it to above that threshold, also shown in Fig. 5.5. It is clear that the extrapolation does not describe the high E_T portion of the distribution well—the extrapolation is simply "too far." In other words, there is a large systematic uncertainty present in extrapolations that use such a small portion of the distribution that the shape can not be reliably obtained. This can be mitigated by raising the E_T threshold, unless

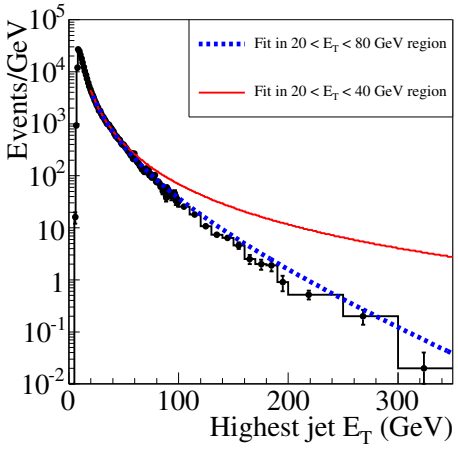

Figure 5.5: E_T of the highest E_T jet in standard model $Z \to \mu\mu$ Monte Carlo events. The distribution is fit to Eq. (5.1) in the region $20 < E_T < 80$ GeV (dotted line), and again in the region $20 < E_T < 40$ GeV (solid line).

the shape of the jet E_T distribution at high E_T can be otherwise constrained. In the case examined in this analysis, we fit the third highest E_T jet (which has a softer E_T distribution than the highest E_T jet) in the region $E_T < 30$ GeV. We have checked that the data in this region constrains the shape sufficiently with validation studies using control samples of data and Monte Carlo simulations.

From the above, it is apparent that one can estimate the background for events with $N_{\rm jet}^X \geq n$ by fitting the E_T distribution of the $n^{\rm th}$ highest E_T jet in the region $E_T < X$ and extrapolating the fit to the region $E_T > X$, as long as the fit region $E_T < X$ constrains the shape sufficiently.

5.4.2 J_T Shape Determination

I now describe the method used to determine the shape of the J_T^{30} distribution of events with $N_{\rm jet}^{30} \geq 3$. After finding the shape, we then normalize it to the number of events with $N_{\rm jet}^{30} \geq 3$ found by the above method. We again use standard model $Z \to \mu\mu$ Monte Carlo events merely to explain the method, and later will apply it to data.

Since J_T^{30} is simply the sum of the individual jet transverse energies above 30 GeV, if we know the E_T distributions of jets for events with $N_{\rm jet}^{30} \geq 3$ we can predict the values of J_T^{30} in these events. We extrapolate the shape of these jet E_T distributions from the jet E_T distributions of $N_{\rm jet}^{30} \leq 2$ events. In order to do such an extrapolation, we must understand the variation of the jet E_T distribution as a function of $N_{\rm jet}^{30}$.

Using $Z \to \ell\ell$ data, we show in Fig. 5.6 the E_T distributions of all jets in events with $N_{\rm jet}^{30} = 1$ and 2, normalized to have equal area. The general shape is similar, though jets in $N_{\rm jet}^{30} = 2$ events have a slightly harder tail at high E_T. We model this by fitting to each jet E_T distribution (using Eq. (5.1)) and extrapolating the fit parameters to $N_{\rm jet}^{30} \geq 3$ events. To avoid simultaneously extrapolating two fit parameters we only extrapolate the exponential parameter (p_1), as this parameter governs the high E_T behavior in our parameterization.

In order to extrapolate only this parameter, we fit the $N_{\rm jet}^{30} = 1$ E_T spectrum allowing both parameters to float freely, then fix the power law parameter (p_2) in the fit to the $N_{\rm jet}^{30} = 2$ E_T spectrum. We then extrapolate the p_1 parameter of Eq. (5.1) linearly as a function of $N_{\rm jet}^{30}$, from their fitted values at $N_{\rm jet}^{30} = 1$ and $N_{\rm jet}^{30} = 2$ into the region $N_{\rm jet}^{30} \geq 3$.

Figures 5.7 and 5.8 show the fits of the spectra for events with 1 and 2 jets. Figure 5.9 shows the linear extrapolation of the exponential parameters. For illustration, we show on the same figure the exponential parameter obtained from a fit to the E_T distribution in $N_{\rm jet}^{30} = 3$ events (again fixing the power law parameter to that found in the $N_{\rm jet}^{30} = 1$ events). The extrapolation reasonably predicts the parameter for events with $N_{\rm jet}^{30} = 3$.[6]

This dependence of the jet E_T spectra on $N_{\rm jet}^{30}$ is modeled as described by our parameter extrapolation, allowing us to predict the shapes of the jet E_T spectra for events with $N_{\rm jet}^{30} \geq 3$. The J_T^{30} distribution is now almost completely determined. We only need an estimate for the relative fractions of events with 3, 4, 5, ... jets. For this, we use an exponential fit parameterization, fit to the $N_{\rm jet}^{30}$ distribution in the region $N_{\rm jet}^{30} \leq 2$, and use this shape in the $N_{\rm jet}^{30} \geq 3$ region. We

[6]As we do not expect many events in data with $N_{\rm jet}^{30} \geq 4$, a detailed checking of the parameter extrapolation to these jet multiplicities is not necessary. We have verified that the extrapolation is consistent with this distribution with the statistics present in Monte Carlo. In addition, this extrapolation is implicitly validated when the validation of the method as a whole is done in Sec. 5.4.4.

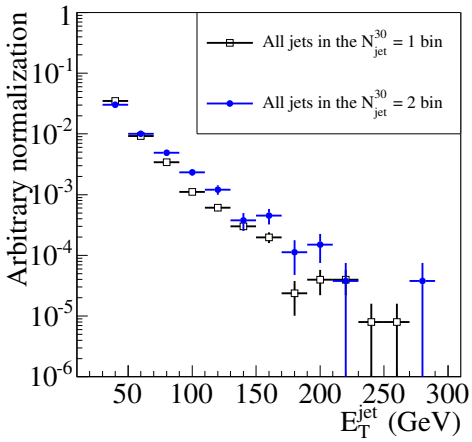

Figure 5.6: E_T distribution of jets in $N_{\text{jet}}^{30} = 1$ events (open squares) and in $N_{\text{jet}}^{30} = 2$ events (solid circles) in $Z \to \ell\ell$ data. Events with higher N_{jet}^{30} have harder the E_T spectra.

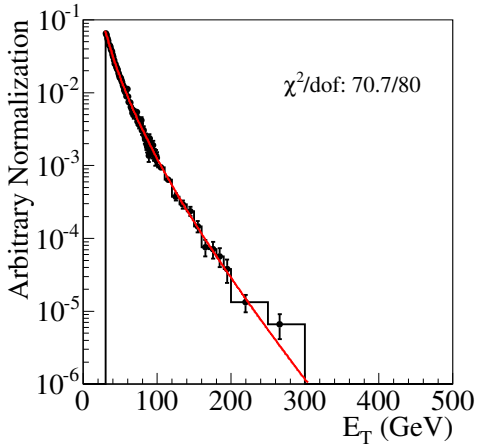

Figure 5.7: E_T distribution of jets in $N_{\text{jet}}^{30} = 1$ events in standard model $Z \to \mu\mu$ Monte Carlo events. The distribution is fit to Eq. (5.1) in the range $E_T > 30$.

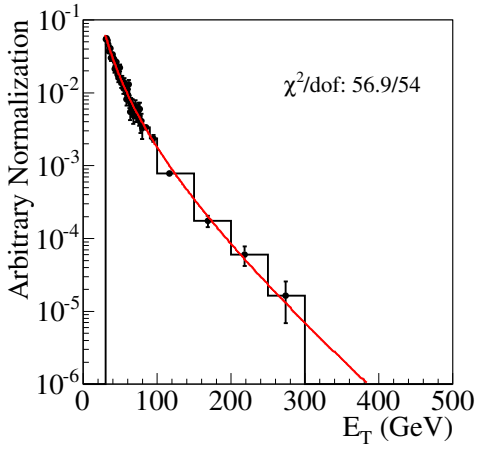

Figure 5.8: E_T distribution of jets in $N_{\rm jet}^{30} = 2$ events in standard model $Z \to \mu\mu$ Monte Carlo events. The distribution is fit to Eq. (5.1) in the range $E_T > 30$, with the parameter p_2 fixed to that obtained from Fig. 5.7.

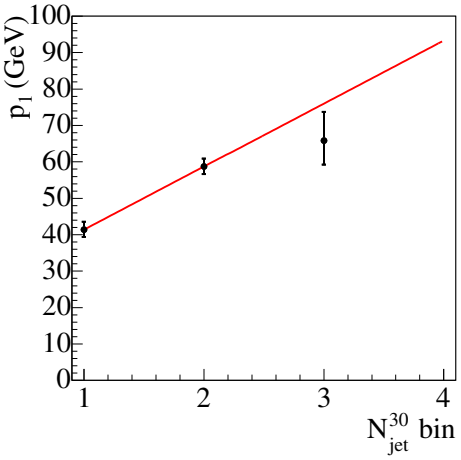

Figure 5.9: The fit value of the exponential parameter p_1 vs. $N_{\rm jet}^{30}$ in standard model $Z \to \mu\mu$ Monte Carlo events.

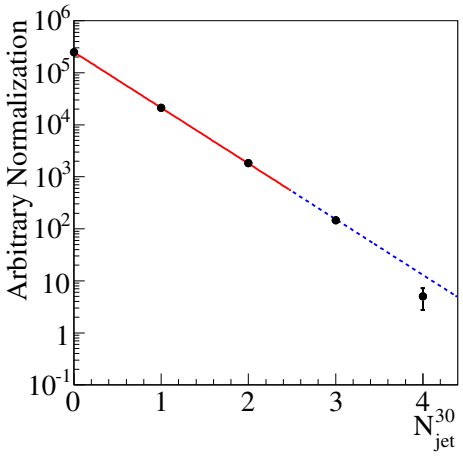

Figure 5.10: $N_{\rm jet}^{30}$ distribution in standard model $Z \to \mu\mu$ Monte Carlo events, fit to an exponential in the range $N_{\rm jet}^{30} \leq 2$. This shape is used to estimate the relative fractions of events with 3, 4, 5, ... jets.

show this fit in Fig. 5.10. There is no theoretical motivation for an exponential shape; we merely use it as an estimate, and verify that the J_T^{30} prediction does not strongly depend on the chosen parameterization. As the total number of events with $N_{\rm jet}^{30} \geq 3$ is already constrained using the method from Sec. 5.4.1, the dependence of the J_T^{30} distribution on the exponential parameterization of the $N_{\rm jet}^{30}$ distribution is small.

Finally, given the above shapes, it is straightforward to make a simple Monte Carlo program that samples these shapes to get the J_T^{30} distribution. The steps required to make this J_T^{30} prediction are:

1. For each event, generate the number of jets by randomly sampling the predicted N_{jet}^{30} distribution in the range $\{3, 4, 5, ...\}$.

2. Take the appropriate jet E_T distribution for this number of jets after extrapolating the exponential fit parameter. Independently sample this jet E_T distribution for each jet.

3. Sum these jets to obtain the J_T^{30}.

The process is repeated as necessary until the J_T^{30} shape is obtained to the desired level of statistical precision.

On step 2, we independently sample the jet E_T shape; however, there is potentially some correlation between the individual jet energies. Including this correlation in the J_T^{30} shape prediction would have the effect of making the tail at large values of J_T^{30} slightly harder. In the validation studies in Sec. 5.4.4 we verify that the correlation is below the level necessary to affect the fit prediction. To understand this further, in Fig. 5.11, we plot the E_T of one the jets versus the other in events with $N_{\text{jet}}^{30} = 2$ in the $Z \to \ell\ell$ data. There is no correlation evident in the plot; we calculate, in the 663 events with $N_{\text{jet}}^{30} = 2$, only a small correlation of 25%, indicating that independently sampling the E_T distribution is a reasonable approximation.

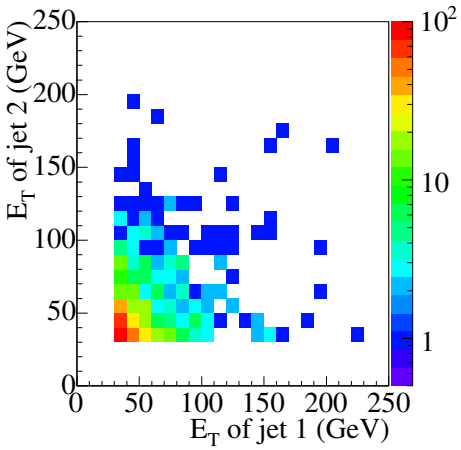

Figure 5.11: The E_T of a random jet vs. the E_T of the other, using jets with $N_{\text{jet}}^{30} = 2$ in $Z \to \ell\ell$ data.

5.4.3 Uncertainties on Fit Prediction

There are two sources of uncertainty on the mean background prediction: the statistical uncertainty from the finite amount of data in the fits, and the systematic uncertainty from imperfect modeling of the various shapes in the fits.

Statistical Uncertainty on Fit Prediction

The third highest E_T jet normalization fit predicts the total number of events with $N_{\text{jet}}^{30} \geq 3$, using the parameter values at the minimum $-\log L$, where L is the likelihood (or equivalently, the maximum likelihood). The 1σ uncertainty on the number of events is simply obtained from its values at the minimum

$-\log L + \frac{1}{2}$. Since the total number of events with $N_{\text{jet}}^{30} \geq 3$ is given by a single fit, its uncertainty is easily determined with this method.

The J_T^{30} prediction is obtained by extrapolating the behavior of multiple distributions, and to estimate its shape uncertainty we vary each fit parameter independently within its uncertainty (output by the fit) and re-do the extrapolation procedure. The individual uncertainties are combined in quadrature to obtain the total uncertainty. The normalization error is then added in quadrature as well to obtain the uncertainty on the fully-normalized J_T^{30} distribution.

Systematic Uncertainty on Fit Prediction

As the background from Z+jet events is determined from a fit to the data, the only source of systematic uncertainties is mis-parameterization of those data. If the data were poorly parameterized, fitting a subset of the data would give a large change in the background prediction. We therefore estimate the size of the mis-parameterization uncertainties by changing the range of each fit and re-doing the fit procedure to obtain the J_T^{30} normalization and shape prediction. Both uncertainties, that on the total number of events with $N_{\text{jet}}^{30} \geq 3$ (from the third highest E_T jet fit), and that on the J_T^{30} shape, are estimated in this way. The variations from each fit range change are then added in quadrature to obtain the full uncertainty. We summarize the fit range changes in Table 5.4. The "$\pm 1\sigma$"

range changes are chosen to give sufficient coverage when observed in control samples of data.

Distribution	nominal range	"-1σ" range	"$+1\sigma$" range
Third highest E_T jet	$(15, 30)$ GeV	$(15, 26)$ GeV	$(17, 30)$ GeV
$N_{\text{jet}}^{30} = 1$ jet E_T	$(30, \infty)$ GeV	$(30, 150)$ GeV	$(70, \infty)$ GeV
$N_{\text{jet}}^{30} = 2$ jet E_T	$(30, \infty)$ GeV	$(30, 80)$ GeV	$(50, \infty)$ GeV
N_{jet}^{30} shape	$[0, 2]$ jets	$[0, 1]$ jets	$[1, 2]$ jets

Table 5.4: Nominal fit ranges and the fit range changes used to estimate systematic uncertainties. The nominal fit range of each distribution is shown in the second column. The third and fourth columns show the ranges used to estimate the uncertainty from a mis-parameterization of that distribution.

Finally, using the technique and the uncertainties developed above in the Monte Carlo simulation, we can demonstrate that the method is self-consistent by checking that the normalized J_T^{30} prediction for events with $N_{\text{jet}}^{30} \geq 3$ matches that observed in Monte Carlo events. We show this comparison in Fig. 5.12. The observed distribution agrees well with the prediction.

5.4.4 Validation of Technique

Having demonstrated and described the procedure for obtaining the Z+jet background using Monte Carlo simulation, I now describe its validation, done predominantly in data. The Z+jet data cannot be used as a validation sample

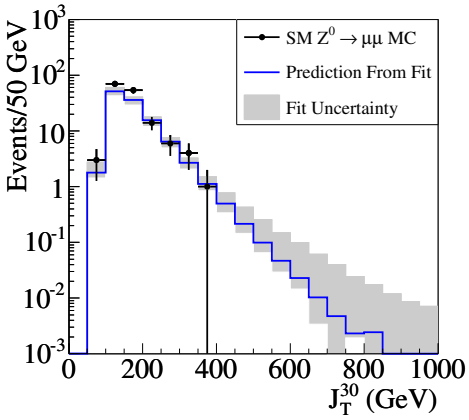

Figure 5.12: The prediction for the J_T^{30} distribution (blue line) of standard model Z Monte Carlo and its uncertainty (gray band), compared to the actual distribution (black points with errors).

because of potential signal bias, so we must test on other data samples. We use two sets of multi-jet data as background-only validation samples, and W+jet data as a background sample containing a real heavy quark signal from $t\bar{t}$ production. Finally, we do signal-injection studies with Monte Carlo simulations to understand the effect of signal bias on the fit procedure.

Multi-Jet Data

The Z+jet background extrapolation only requires information about the jet E_T distributions, and not the Z. It should therefore perform similarly well not only for Z+jet events, but "X"+jet events, provided that the "X" has a similar

transverse momentum spectrum as the Z. That is, if the "X" has, for example, a minimum p_T threshold, the E_T distributions of the jets will be sculpted such that they no longer follow the power law $\times$ exponential parameterization of Eq. (5.1).

We first obtain "X"+jet events from multi-jet data dominated by QCD interactions using prescaled jet triggers that require at least one jet with $E_T > 20$ GeV.[7] An "X" is then made by picking two random jets in the event, requiring they both have $E_T > 20$ GeV (to match the electron and muon p_T cuts), and requiring $M_X > 70$ GeV/c^2 to remove the invariant mass turn-on. The invariant mass is not further restricted to the region $81 < M_X < 101$ GeV/c^2 to maximize statistics; in any case the J_T^{30} distribution is observed to not depend on M_X in this sample.

Given this "X" selection, we use the remaining jets in the event to validate the procedure. Figure 5.13 shows the third highest E_T jet distribution. We extrapolate this distribution above 30 GeV using Eq. (5.1). We obtain a prediction of 97^{+27}_{-27} (stat. error only) events with $N_{\rm jet}^{30} \geq 3$. We observe 80 events. This is clearly consistent within the uncertainties. To quantitatively evaluate the level of consistency we calculate the probability to measure the observed number of

[7]Since the cross section for jet events with $E_T > 20$ GeV is extremely large, not all events of this type are able to be kept by the data acquisition system. Only a fraction of these events are kept; the inverse of the fraction of events kept is known as the prescale. For the single jet trigger with $E_T > 20$ GeV, the total prescale used is approximately 500.

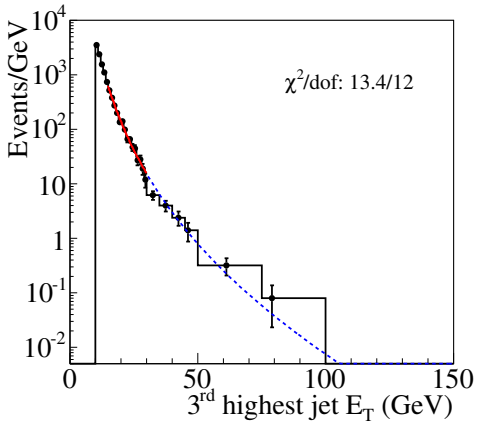

Figure 5.13: E_T distribution of the third highest E_T jet in "X"+jet events selected with the jet triggers as described in the text. The distribution is fit to Eq. (5.1) in the $15 < E_T < 30$ GeV region and extrapolated to the $E_T > 30$ GeV region.

events or higher given the background prediction, as well as convert this probability to units of standard deviations[8]. This calculation gives a corresponding probability of 0.73; this is a 0.6σ level of consistency.

[8]This probability calculation is done by integrating the distribution of the expected number of events above the observed value. For the distribution of the expected number of events, we use a Poisson distribution with a mean equal to the fit prediction (97 in this case) smeared with a Gaussian centered at zero with a width equal to the background prediction's uncertainty ($^{+27}_{-27}$ in this case). If the number of data events is higher than the background prediction, we use the upper uncertainty in the Gaussian smearing; we use the lower uncertainty if the data is below the background prediction. Additionally we convert this probability to units of standard deviation by inverting:

$$\int_n^\infty \frac{1}{\sqrt{2\pi}} e^{-x^2/2} dx = p$$

We now predict the J_T^{30} shape. Figures 5.14 and 5.15 show the fits to the jet E_T spectra for events with $N_{\rm jet}^{30} = 1$ and 2. We extrapolate the parameter p_1 using the plot in Fig. 5.16 to events with $N_{\rm jet}^{30} \geq 3$. The $N_{\rm jet}^{30}$ shape is taken from the fit in Fig. 5.17. Using these ingredients we run the simple Monte Carlo program to obtain the J_T^{30} shape, and normalize it to the prediction of 97 events for $N_{\rm jet}^{30} \geq 3$. The prediction and total uncertainty is shown overlaid with the actual distribution in "X"+jet data in Fig. 5.18. The distribution clearly agrees well within the uncertainty envelope.

Because the J_T^{30} uncertainties in each bin are correlated, an independent data to background comparison in each bin is not straightforward. Rather, we test the shape agreement once using the (arbitrarily chosen) region of $J_T^{30} > 200$ GeV. Above 200 GeV, we expect $19.7^{+9.2}_{-9.0}$ events and observe 20 events.

The background extrapolation method predicts within its uncertainties the normalization and shape of the J_T^{30} distribution in the jet triggered sample. However, because of the prescale, this sample has relatively low statistics despite the large cross section of QCD multi-jet processes. To obtain a higher statistics sample of multi-jet data, we can use the electron triggers, which are not prescaled. In this sample we construct an "X" by pairing the triggered electron with a "fake" electron, which is an EM calorimeter cluster that is reconstructed as an electron but fails the low hadronic energy requirement. "X" events selected in

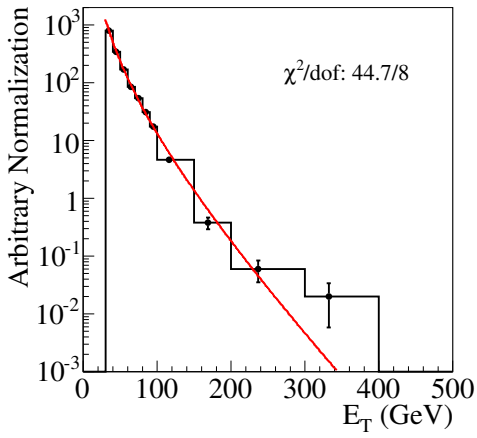

Figure 5.14: E_T distribution of jets in $N_{\text{jet}}^{30} = 1$ "X"+jet events, selected with the jet triggers as described in the text. The distribution is fit to Eq. (5.1) in the $E_T > 30$ GeV region.

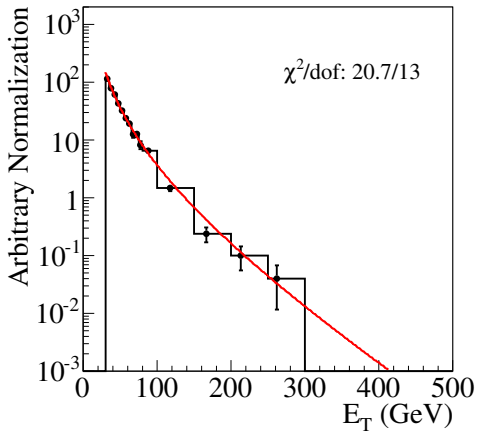

Figure 5.15: E_T distribution of jets in $N_{\rm jet}^{30} = 2$ "X"+jet events selected with the jet triggers as described in the text. The distribution is fit to Eq. (5.1) in the $E_T > 30$ GeV region with the parameter p_2 fixed to that obtained from the fit in Fig. 5.14.

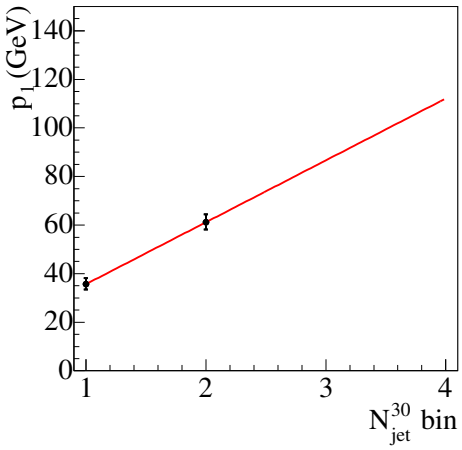

Figure 5.16: The fit value of the exponential parameter p_1 vs. $N_{\rm jet}^{30}$ in "X"+jet events selected with the jet triggers as described in the text.

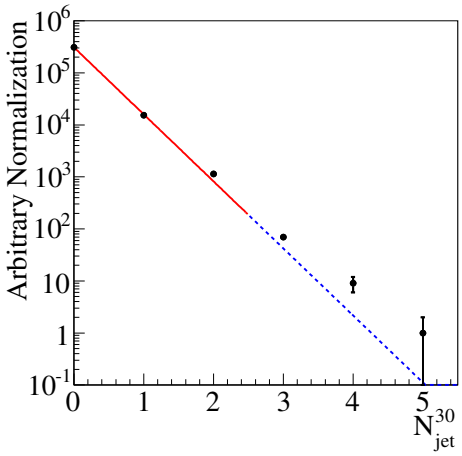

Figure 5.17: $N_{\rm jet}^{30}$ distribution in "X"+jet events selected with the jet triggers as described in the text. The distribution is fit to an exponential in the range $N_{\rm jet}^{30} \leq 2$.

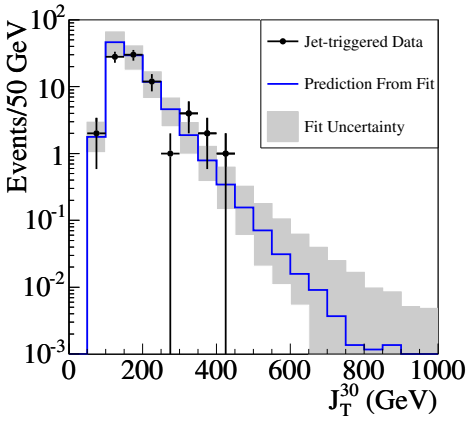

Figure 5.18: The prediction (blue line) and uncertainty (gray band) for the J_T^{30} distribution of "X"+jet events selected with the jet triggers as described in the text. The prediction is compared to the actual distribution (black points with errors). The observation agrees with the prediction.

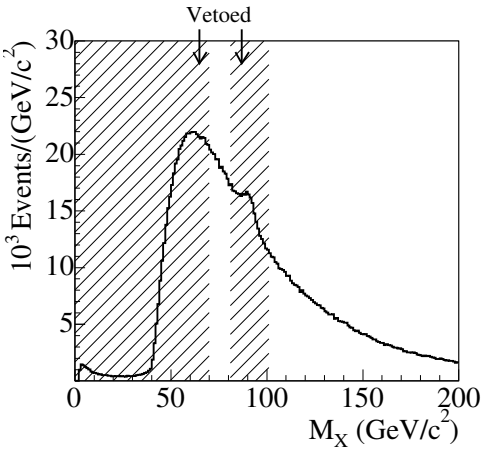

Figure 5.19: Distribution of M_X in "X"+jet events selected from the electron triggers as described in the text. The shaded regions are removed; that is, events with $M_X > 70$ GeV/c^2 are selected, and the $81 < M_X < 101$ GeV/c^2 region is vetoed.

this way are dominated by QCD dijet events in which both jets fake electron candidates. Again, we require $M_X > 70$ GeV/c^2 to remove the invariant mass turn-on. Additionally the invariant mass region $81 < M_X < 101$ GeV/c^2 is vetoed to remove real $Z \to ee$ events. Figure 5.19 shows the plot of the invariant mass before these requirements.

Given this "X" selection, we use the remaining jets in the event to validate the procedure. Figure 5.20 shows the third highest E_T jet distribution. We extrapolate this distribution above 30 GeV using Eq. (5.1). We obtain a predic-

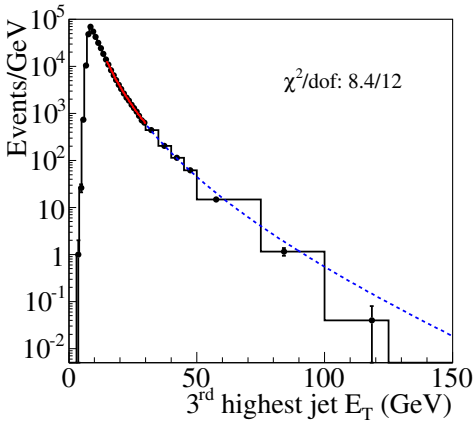

Figure 5.20: E_T distribution of the third highest E_T jet in "X"+jet events selected with the electron triggers as described in the text. The distribution is fit to Eq. (5.1) in the $15 < E_T < 30$ GeV region and extrapolated to the $E_T > 30$ GeV region.

tion of 4427^{+354}_{-310} (stat. error only) events with $N^{30}_{\rm jet} \geq 3$. We observe 4509 events. Approximating the Poisson distribution of the number of observed events as a Gaussian, this is a 0.23σ level of consistency.

We predict the J^{30}_T shape using the usual procedure of extrapolating the jet E_T distributions from events with $N^{30}_{\rm jet} = 1$ and 2 to $N^{30}_{\rm jet} \geq 3$. The normalized prediction and its uncertainty are compared to the actual distribution in the data in Fig. 5.21. The distribution agrees well within the uncertainty envelope. Above 200 GeV, we expect 1412^{+477}_{-212} events; we observe 1128 events, for a -1.3σ level of consistency. We compare the background prediction to the number of

observed events as a function of the J_T^{30} cut in Table 5.5. The prediction agrees well over the entire J_T^{30} distribution.

Minimum J_T^{30} cut	Total Bkg. (events)	Data (events)
50	4430^{+1270}_{-600}	4509
100	4380^{+1250}_{-590}	4463
150	2810^{+830}_{-360}	2602
200	1410^{+480}_{-210}	1128
250	667^{+281}_{-133}	436
300	$312^{+172}_{-81.8}$	170
350	$146^{+106}_{-47.4}$	62
400	$68.7^{+64.8}_{-26.2}$	27
450	$32.8^{+38.9}_{-14.3}$	15
500	$16.2^{+23.3}_{-8.4}$	6
550	$7.9^{+14.5}_{-4.5}$	3
600	$3.9^{+8.8}_{-2.5}$	0

Table 5.5: The "X"+jet data (selected with the electron triggers as described in the text) vs. J_T^{30}, compared with the background prediction.

We have seen that the background extrapolation performs well enough in this high-statistics validation sample. Because of the high-statistics, we are able to divide this sample into subsamples and test the prediction method many times over and test the uncertainties. The multi-jet data is divided into 50 subsamples to check the background estimation with the number of events expected in the Z+jet data.

To validate the third highest E_T jet extrapolation, we evaluate the consistency between the fit prediction and the observation in each subsample. We

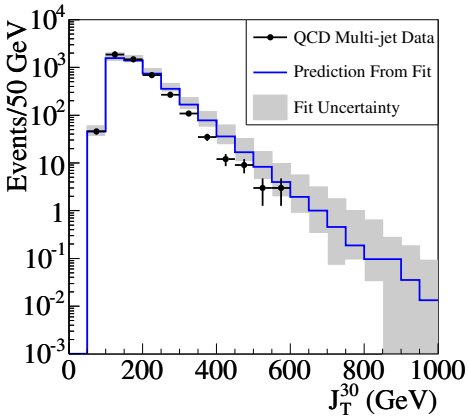

Figure 5.21: The prediction (blue line) and uncertainty (gray band) for the J_T^{30} distribution of "X"+jet events selected with the electron triggers as described in the text. The prediction is compared to the actual distribution (black points with errors). The observation agrees with the prediction, with the a maximum fluctuation downward of 1.9σ. The data are below the prediction for several point because the shape uncertainty is correlated between bins.

observe that the pull distribution from these calculations is consistent with a Gaussian with mean 0 and width of 1, indicating that the mean prediction and the uncertainties are correctly calculated for the $N_{\text{jet}}^{30} \geq 3$ prediction. On average, the background prediction is $3 \pm 5\%$ low relative to the data. That is, the background prediction underestimates the background, but by an amount consistent with zero. This is consistent with the fit done in standard model Z Monte Carlo simulation in Sec. 5.4.1, in which the background prediction was $31 \pm 16\%$ low relative to the data.

To validate the J_T^{30} shape prediction, in each subsample we evaluate the consistency between the fit prediction and the observation using a cut of $J_T^{30} > 200$ GeV. In this case, the resulting pull distribution was inconsistent with a Gaussian with mean 0 and width 1. We find that the background prediction overestimates the number of observed events, and that the uncertainty is overly conservative, after correcting for this bias. On average, the background prediction is $23 \pm 7\%$ high relative to the data. However, we found that this bias was covered by the uncertainties, with an average uncertainty on the background prediction of 47%. To clarify, these biases are only present in the J_T^{30} shape prediction, and not in the $N_{\text{jet}}^{30} \geq 3$ prediction.

To compare the jet kinematics in each of the validation samples (both the "X" events selected from jet triggers and the "X" events selected from the electron

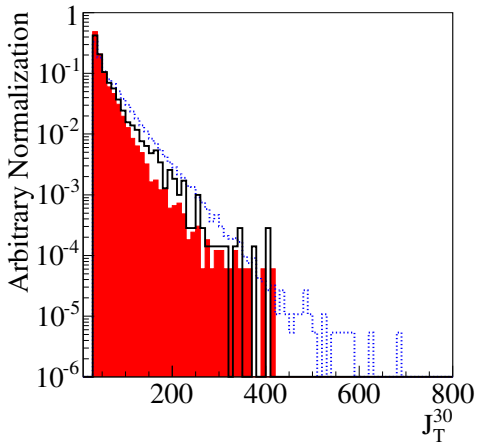

Figure 5.22: The J_T^{30} distribution without the $N_{\text{jet}}^{30} \geq 3$ requirement in the Z+jet data (black line), compared to "X"+jet data selected with the jet triggers (red histogram) and to "X"+jet data selected with the electron triggers (dotted blue line).

triggers) to the Z+jet data, we plot the J_T^{30} distribution of each, without the $N_{\text{jet}}^{30} \geq 3$ requirement, in Fig. 5.22. The overall shape of each is the same, although they are slightly different—for example, electron-triggered "X"+jet data have a harder spectrum. However, the background estimation takes these differences into account in the fit procedure.

These validations show that the fit prediction method correctly calculates the background when there is no signal present. To verify that it calculates the background correctly in the presence of signal, we use W+jet data.

W+jet Data

The tree-level single W diagrams and the physics that gives rise to additional jets is similar to Z+jet production, and so we expect similar behavior in the W+jet data. However in the W+jet data, in addition to the single-W production there is also a heavy quark signal from the top quark, producing W bosons via $t\bar{t} \rightarrow WWb\bar{b}$. This sample provides a useful and interesting validation of the method—it is a real data sample that can test whether or not the background fit procedure performs properly in the presence of a signal similar to that of the search.

We select W events in the $W \rightarrow \mu\nu$ channel by requiring exactly one "tight" muon and missing transverse energy ($\not\!\!E_T$). The $\not\!\!E_T$ is measured using the vector sum of the calorimeter tower transverse energies and the muon p_T. We require $\not\!\!E_T > 25$ GeV. Since we are requiring only a single muon, we are using the so-called "lepton+jets" channel of the top quark selected with only kinematic information, and without tagging b-jets [36].

Using this W+jet selection, we test the extraction of the top signal for events with $N_{\rm jet}^{30} \geq 3$ using only data as a validation of the method for predicting the Z+jet background. We expect standard model W+jet to be the dominant background for $t\bar{t}$ after the $N_{\rm jet}^{30}$ requirement. In single W+jet Monte Carlo simulation with no $t\bar{t}$ component, the method does predict the actual Monte

Carlo distribution well. We then apply the same method to the W+jet data, fitting the third highest E_T jet distribution to Eq. (5.1) in Fig. 5.23. In this case, the extrapolation does not describe the data well.

The extrapolation predicts 439^{+20}_{-20} (stat.) $^{+30}_{-24}$ (syst.) events; we observe 762 events. We make the hypothesis that this excess is due to the top quark, and test this by checking that the cross section is consistent with that expected for $t\bar{t}$. The excess of the data above the background gives the number of $t\bar{t}$ candidates, 323^{+34}_{-34} (stat.) $^{+30}_{-24}$ (syst.). Using $t\bar{t}$ Monte Carlo events gives an estimate for the acceptance×efficiency of $3.41 \pm 0.02\%$. The luminosity of the muon-triggered sample is 1.04 fb^{-1}. We therefore obtain a cross section of 9 ± 1 pb (stat. uncert. only)[9]. The proximity to the previous measured cross section in this channel at CDF using 194 pb^{-1}, 6.6 ± 1.1 (stat.) $\pm$ 1.5 (syst.) pb [36], indicates that the excess is consistent with the background+$t\bar{t}$ hypothesis, and that the fit procedure is accurately predicting the background from single W+jet production in the presence of signal.

We now predict the J^{30}_T shape of the W+jet background. Figures 5.24 and 5.25 show the fits to the jet E_T spectra for events with $N^{30}_{\rm jet} = 1$ and 2;

[9]The statistical uncertainty is simply the statistical uncertainty on the background prediction added in quadrature with the statistical uncertainty on the number of observed events, $\sqrt{762}$. We do not give a full systematic uncertainty, as we do not evaluate the uncertainty on the acceptance of $t\bar{t}$. The systematic uncertainty on the cross section from the background prediction alone is 1.5 pb.

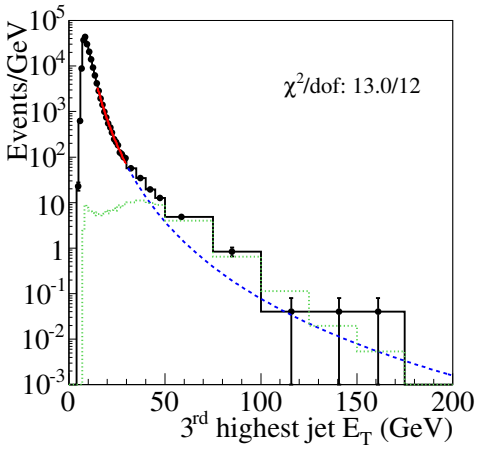

Figure 5.23: E_T distribution of the third highest E_T jet in W+jet events (black line and points). The distribution is fit to Eq. (5.1) in the $15 < E_T < 30$ GeV region and extrapolated to the $E_T > 30$ GeV region. The dotted green line shows the contribution from $t\bar{t}$ at the "measured" cross section of 9 pb. There is very little contribution from $t\bar{t}$ within the fit region. The extrapolated distribution is inconsistent with the background-only hypothesis, but consistent with the background plus $t\bar{t}$ hypothesis.

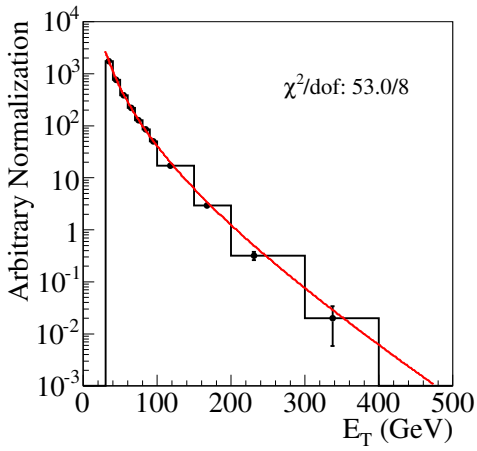

Figure 5.24: E_T distribution of jets in $N_{\rm jet}^{30} = 1$ W+jet events. The distribution is fit to Eq. (5.1) in the $E_T > 30$ GeV region.

Fig. 5.26 shows the parameter p_1 extrapolation; Fig. 5.27 shows the $N_{\rm jet}^{30}$ shape fit. We use these shapes to obtain the J_T^{30} shape and errors, add the expected contribution from $t\bar{t}$ using Monte Carlo simulation (normalized to the "measured" cross section of 9 pb), and compare this to the actual distribution in data in Fig. 5.28. The data is well described by the total J_T^{30} prediction, verifying that the fit procedure can predict the J_T^{30} shape of the background in the presence of signal.

While the predicted shape of the J_T^{30} distribution agrees with the data well (after adding the expected contribution from $t\bar{t}$), the total uncertainty on the background prediction becomes extremely large at high J_T^{30}. The J_T^{30} distribution

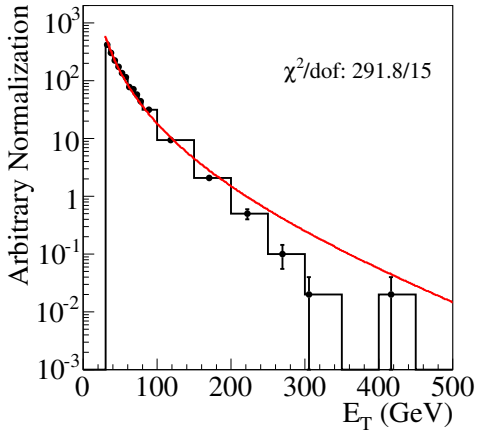

Figure 5.25: E_T distribution of jets in $N_{\rm jet}^{30} = 2$ W+jet events. The distribution is fit to Eq. (5.1) in the $E_T > 30$ GeV region with the parameter p_2 fixed to that obtained from the fit in Fig. 5.24.

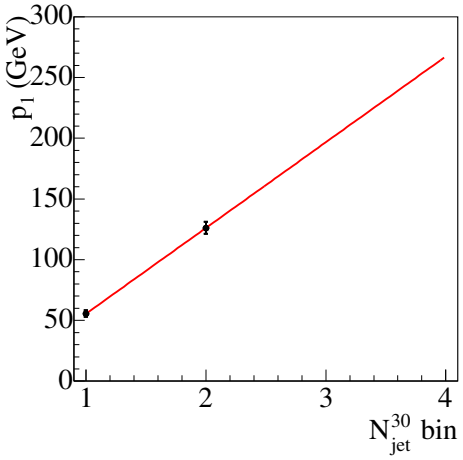

Figure 5.26: The fit value of the exponential parameter p_1 vs. $N_{\rm jet}^{30}$ in W+jet events.

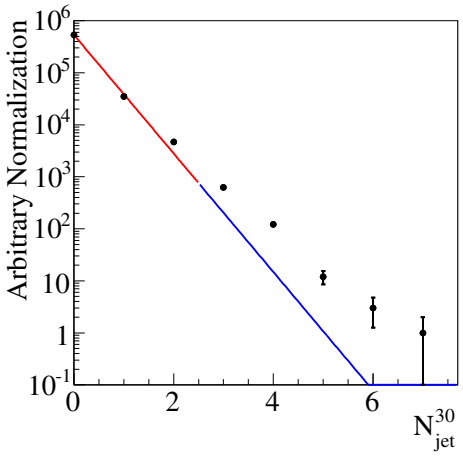

Figure 5.27: $N_{\rm jet}^{30}$ distribution in W+jet events. The distribution is fit to an exponential in the range $N_{\rm jet}^{30} \leq 2$.

for $t\bar{t}$ peaks near 200 GeV, where the uncertainty is small, but it is instructive to understand the reason for the increased uncertainty at very large J_T^{30}. This large error is completely dominated by a poor parameterization of the E_T distribution of jets in $N_{\rm jet}^{30} = 2$ events. Since, in Fig. 5.25, the fitted parameterization poorly describes the data, changing the range from nominal (our method for determining the size of the mis-parameterization uncertainty) will make a large difference in the fit. However, this is not a problem with the parameterization in Eq. (5.1), because if we fit the same spectrum without fixing the power law parameter to the value observed in events with $N_{\rm jet}^{30} = 1$, we get the quite reasonable fit shown in Fig. 5.29. That is, the parameterization still describes the $N_{\rm jet}^{30} = 2$ E_T

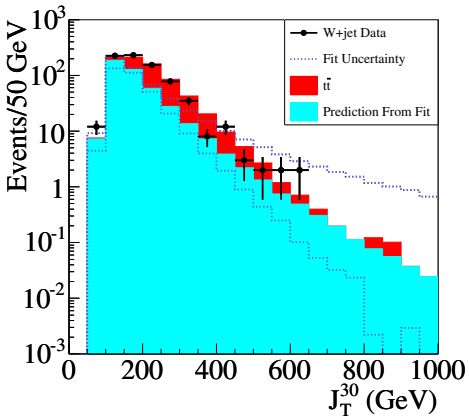

Figure 5.28: The prediction (cyan histogram) and uncertainty (dotted lines) for the J_T^{30} distribution of W+jet events. The expectation from $t\bar{t}$ is added to the prediction. The data (points with errors) agree with the background plus $t\bar{t}$ hypothesis.

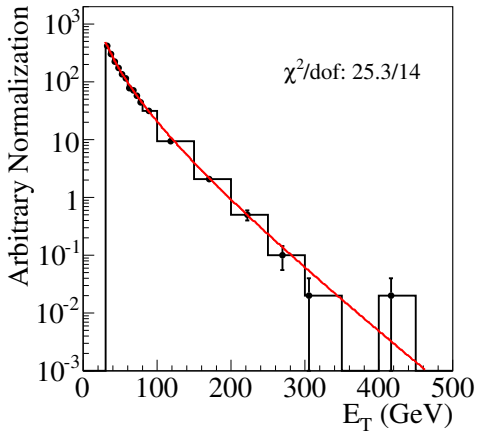

Figure 5.29: E_T distribution of jets in $N_{\rm jet}^{30} = 2$ W+jet events. The distribution is fit to Eq. (5.1) in the $E_T > 30$ GeV region without fixing the the parameter p_2.

spectrum well, but our method of fixing the power law parameter in this fit to that observed from the $N_{\rm jet}^{30} = 1$ E_T spectrum does not describe the behavior of the changing jet E_T distributions as a function of $N_{\rm jet}^{30}$ well in this sample. In the other validation samples in data and Monte Carlo simulations, and particularly in the fits of the Z+jet data, we see no such large systematic effect from a mis-parameterization in the $N_{\rm jet}^{30} = 2$ E_T distribution. This issue therefore does not effect this analysis, but it suggests the background prediction procedure could be enhanced with a more sophisticated parameter extrapolation, perhaps by extrapolating both parameters p_1 and p_2 simultaneously.

Signal Injection Studies

The studies in data indicate the fit method adequately predicts the background, without and with the presence of signal. We would also like to understand at what point, if any, signal contamination causes an unacceptably large change to the background prediction. That is, we need to verify that the background extrapolation does not "fit-away" the signal, as the jet E_T distributions may be substantially changed if there is a large amount of signal in the fitted regions.

To study this effect we use standard model Monte Carlo events with $b' \rightarrow bZ^0$ Monte Carlo events added at a variety of signal masses. We run over an equivalent luminosity of 1 fb^{-1} of Monte Carlo events to understand the effect with the approximate amount of statistics that is present in the data. For this study we use $BR(b' \rightarrow bZ^0) = 100\%$; reducing this branching ratio will only reduce the effect of a signal bias.

For example, the predicted J_T^{30} distributions, done with and without $m_{b'} =$ 200 GeV/c^2 Monte Carlo signal events added to the Z+jet background, are shown in Fig. 5.30. The difference between the background predictions with and without signal is small compared to the actual number of Monte Carlo events, indicating that signal does not bias the fit to a large degree at this mass point.

As expected, as the b' mass increases the fit becomes less biased from the presence of signal; as the b' mass decreases, the fit becomes more biased. At a b' mass of 150 GeV/c^2, we found an increase in signal bias, but sensitivity to this mass point is still retained (at a significance of 4.8σ). At a b' mass of 100 GeV/c^2, however, we found that the signal was completely fit away. We therefore do not set limits below 150 GeV/c^2. We note that we are still sensitive to models with masses near 100 GeV/c^2, as long as the cross sections are sufficiently small. In general, though, lower masses produce more signal contamination than higher masses, as both the cross sections are larger and the E_T distributions have larger fractions within the fit regions. Sensitivity to these lower masses could be increased by lowering E_T thresholds and $N_{\rm jet}$ cuts, and applying similar fit procedures with the altered selection.

5.4.5 Application of Technique to the Signal Sample

We now apply the fit technique to the combined $Z \to ee$ and $Z \to \mu\mu$ data to predict the background from Z+jet final states. The third highest E_T jet distribution is shown in Fig. 5.31, with events that have $N_{\rm jet}^{30} \geq 3$ removed. We fit in the region $15 < E_T < 30$ GeV, and extrapolate to the region $E_T > 30$ GeV. We predict $72.2^{+9.8}_{-11.1}$ events with $N_{\rm jet}^{30} \geq 3$.

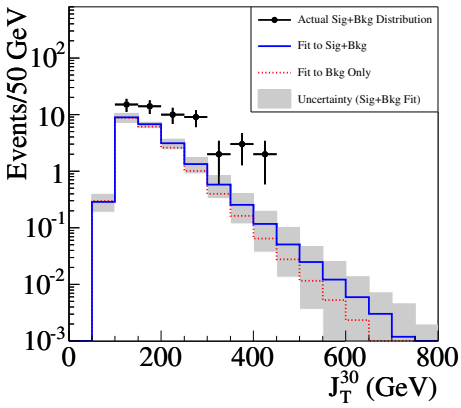

Figure 5.30: Prediction for the J_T^{30} distribution in standard model $Z \rightarrow \mu\mu$ events, with and without the presence of a 200 GeV/c^2 b' signal introduced. The difference between the two predictions is small compared to the excess of signal at large J_T^{30}.

To obtain the J_T^{30} shape of the Z+jet background, we fit the jet E_T distributions of events with $N_{\rm jet}^{30} = 1$ and 2, and linearly extrapolate the fit parameter p_1 to events with $N_{\rm jet}^{30} \geq 3$. We show the fit to the $N_{\rm jet}^{30} = 1$ jet E_T spectrum in Fig. 5.32, the fit to the $N_{\rm jet} = 2$ jet E_T spectrum in Fig. 5.33, and the extrapolation of the fit parameter in Fig. 5.34. We use the fit to the $N_{\rm jet}^{30}$ distribution in the 0, 1, and 2 jet bins in Fig. 5.35 as an estimate of the shape of the $N_{\rm jet}^{30}$ distribution in the 3 and higher jet bins. With these ingredients we run the simple Monte Carlo program to obtain the expected J_T^{30} shape, which is then normalized to the prediction for the total number of $N_{\rm jet}^{30} \geq 3$ background events, $72.2^{+9.8}_{-11.1}$. We show the J_T^{30} distribution prediction and its total statistical+systematic uncertainty in Fig. 5.36.

5.5 Remaining Backgrounds

After having estimated the contribution from Z+jet with the above technique, we now estimate the remaining backgrounds listed in Sec. 5.3.

The second background, multi-jet fakes, has approximately the same shape as the Z+jet background, and is therefore included in the fit procedure. This shape similarity is demonstrated when validating the procedure using multi-jet

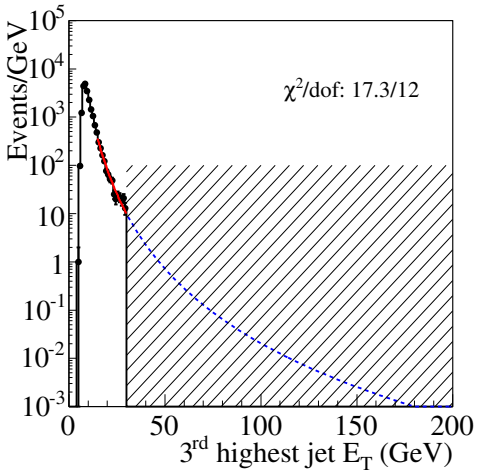

Figure 5.31: E_T distribution of the third highest E_T jet in $Z \to ee$ and $Z \to \mu\mu$ events with $N_{\text{jet}}^{30} \leq 2$. The distribution is fit to Eq. (5.1) in the $15 < E_T < 30$ GeV region and extrapolated to the $E_T > 30$ GeV region. Events with $N_{\text{jet}}^{30} \geq 3$ (equivalent to $E_T > 30$ GeV, the hatched region) are removed from the distribution.

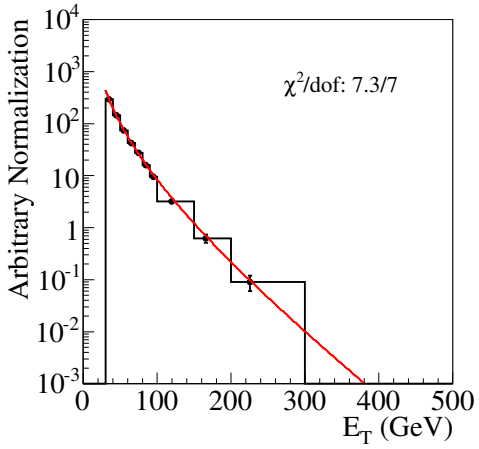

Figure 5.32: E_T distribution of jets in $N_{\rm jet}^{30} = 1$ $Z \to ee$ and $Z \to \mu\mu$ events. The distribution is fit to Eq. (5.1) in the $E_T > 30$ GeV region.

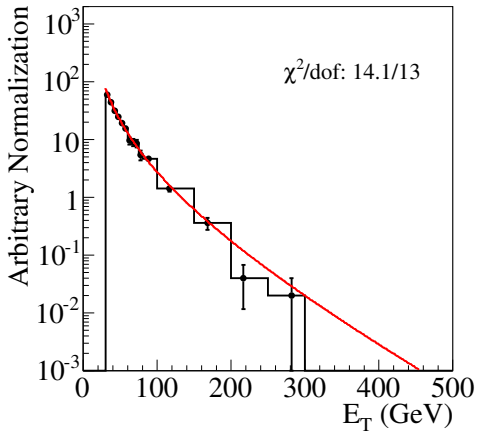

Figure 5.33: E_T distribution of jets in $N_{\rm jet}^{30} = 2$ $Z \to ee$ and $Z \to \mu\mu$ events. The distribution is fit to Eq. (5.1) in the $E_T > 30$ GeV region with the parameter p_2 fixed to that obtained from the fit in Fig. 5.32.

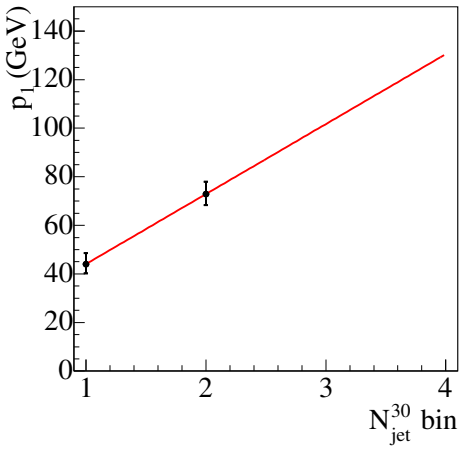

Figure 5.34: The fit value of the exponential parameter p_1 vs. N_{jet}^{30} in $Z \to ee$ and $Z \to \mu\mu$ events.

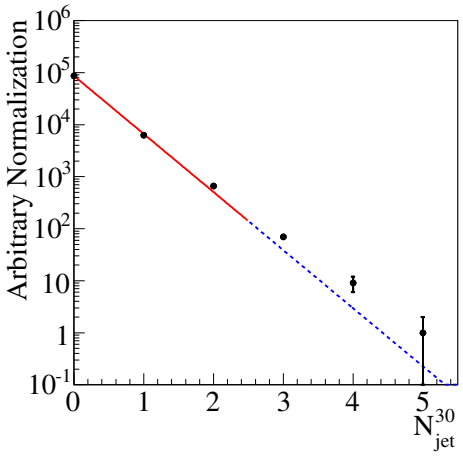

Figure 5.35: N_{jet}^{30} distribution in $Z \to ee$ and $Z \to \mu\mu$ events. The distribution is fit to an exponential in the range $N_{\text{jet}}^{30} \leq 2$.

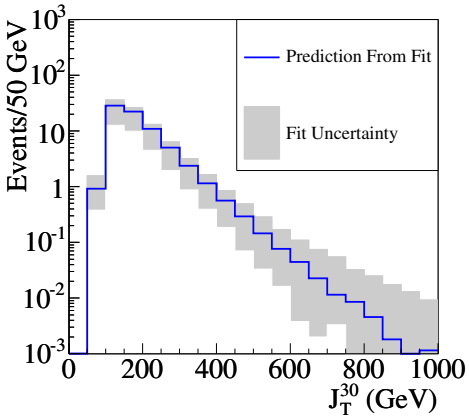

Figure 5.36: The prediction (blue line) and uncertainty (gray band) for the J_T^{30} distribution of $Z \to ee$ and $Z \to \mu\mu$ events.

data in Sec. 5.4.4 above. Since this background is already included in the Z+jet background estimate, no further determination of it is needed.

Nonetheless, we independently measure its size to confirm that it is small relative to the Z+jet background. To obtain an upper bound on the multi-jet background, we use the sidebands of the $M_{\ell\ell}$ distribution for events with $N_{\rm jet}^{30} \geq 3$. We attribute all of the events in the sidebands to multi-jet fakes, and interpolate from the sidebands into the $81 < M_{\ell\ell} < 101$ GeV/c^2 region. Using this method, we estimate less than 11 ± 2 events from multi-jet fakes. Its small size relative to the Z+jet background ($72.2^{+9.8}_{-11.1}$) reinforces our confidence that it warrants no extra attention beyond the fit.

While the third background, from multi-jet events occurring simultaneously with cosmic rays, is also included in the fit procedure as the jet E_T spectra are similar to the Z+jet background, we again independently measure its size. We reject this background using timing information from the COT. We also use this information to estimate this background using the number of events rejected with the timing cut, combined with a measurement of the rejection efficiency in a sample of cosmic rays with high-purity. We find a completely negligible background of $0^{+0.001}_{-0}$ events.

The remaining backgrounds are not included in the fit procedure since they contain jets from the decays of massive particles and so the jet E_T spectra do not follow the parameterization in Eq. (5.1). They can be estimated with Monte Carlo simulations normalizing to the expected standard model cross sections. All remaining backgrounds are negligible relative to the Z+jet background, the largest being from WZ, with an estimated contribution of 1.6 ± 0.1 events. Each of the background contributions to the $N^{30}_{\rm jet} \geq 3$ region is summarized in Table 5.6. As the backgrounds from WZ, ZZ, and $t\bar{t}$ are negligible compared to the Z+jet background, they are excluded in the background estimation vs. J^{30}_T.

Process	Background
Z+jet	$72.2^{+9.8}_{-11.1}$
Multi-jet fakes	$< 11 \pm 2$ (included in Z+jet fit)
Cosmics	$0^{+0.001}_{-0}$
WZ	1.6 ± 0.1
ZZ	0.7 ± 0.1
$t\bar{t}$	0.8 ± 0.1
Total	$75.3^{+9.8}_{-11.1}$

Table 5.6: Summary of all backgrounds after selecting events with $N_{\rm jet}^{30} \geq 3$, independent of J_T^{30}.

5.6 Results

We now compare the background prediction to the observation in the Z+jet data. From the third highest E_T jet extrapolation, we predict $75.3^{+9.8}_{-11.1}$ events with $N_{\rm jet}^{30} \geq 3$, and observe 80 events. In Fig. 5.37, we show the extrapolation overlaid with the data. The data agree with the extrapolation well. We compare the predicted J_T^{30} distribution to that observed in data in Fig. 5.38. Again, the data agree with the prediction quite well. We list the predicted and observed number of events integrated above various J_T^{30} cuts in Table 5.7. We search for an excess above the prediction at each J_T^{30} cut value. Even when ignoring the systematic uncertainties, the maximum difference upward has a significance of $+0.9\sigma$; the maximum difference downward has a significance of -1.4σ.

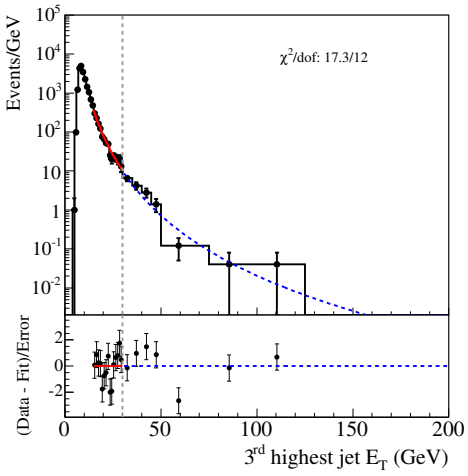

Figure 5.37: E_T distribution of the third highest E_T jet in $Z \to ee$ and $Z \to \mu\mu$ events. The fit from Fig. 5.31 is overlaid. The fit extrapolation matches the distribution above 30 GeV well.

Given that there is no significant excess present in the data, we set a cross section limit using the fourth generation model. At each b' mass, the counting experiment is evaluated with the requirement $J_T^{30} > m_{b'}c^2$. The limit is set at a 95% confidence level by integrating a likelihood obtained using a Bayesian technique that smears the Poisson-distributed background with Gaussian acceptance and mean background uncertainties [37]. The background and its uncertainty are taken from the fit prediction (listed in Table 5.7); the acceptance×efficiency is taken from Monte Carlo simulation, with correction factors applied to match the observed efficiency of leptons in $Z \to \ell\ell$ data. The uncertainty on the

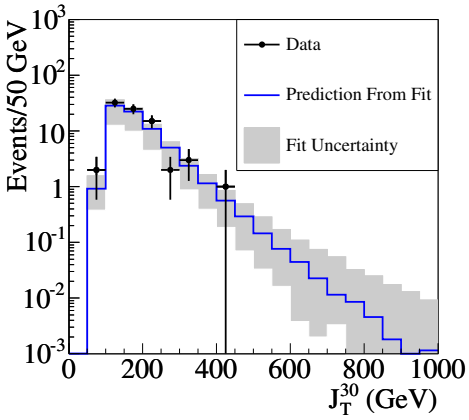

Figure 5.38: The J_T^{30} prediction and uncertainty from Fig. 5.36 compared to the observed distribution (black points and errors) in $Z \to ee$ and $Z \to \mu\mu$ events with $N_{\text{jet}}^{30} \geq 3$. The prediction agrees well with the data.

acceptance×efficiency is 10%, with the dominant source from a jet energy scale uncertainty of 6.7% [33], the second dominant from a luminosity uncertainty of 5.9%, and the remainder from Monte Carlo event statistics and imperfect knowledge of lepton identification efficiencies [38], parton distribution functions [27], and initial and final state radiation.

The 95% confidence level cross section limit as a function of mass is shown in Fig. 5.39. In models with different acceptances, the acceptances of the fourth generation model (for these values, see Table 5.8) simply need to be factored out and the acceptances of those models should be included.

Minimum J_T^{30} cut	Total Bkg. (events)	Data (events)
50	$72.2^{+17.9}_{-41.3}$	80
100	$71.3^{+17.3}_{-40.7}$	78
150	$42.8^{+9.6}_{-24.8}$	46
200	$20.6^{+5.6}_{-12.6}$	21
250	$9.7^{+3.6}_{-6.2}$	6
300	$4.7^{+2.3}_{-3.1}$	4
350	$2.3^{+1.5}_{-1.6}$	1
400	$1.2^{+1.0}_{-0.9}$	1
450	$0.6^{+0.7}_{-0.5}$	0
500	$0.3^{+0.5}_{-0.3}$	0

Table 5.7: The data compared to the Z+jet background fit prediction vs. J_T^{30}.

To set a mass limit on the fourth generation model, we calculate the b' cross section at leading order using PYTHIA, with the assumption that $BR(b' \to bZ) = 100\%$. With this assumption, the mass limit observed is $m_{b'} > 268$ GeV/c^2. The previous search on this model in the bZ channel obtained a limit of $m_{b'} > 199$ GeV/c^2 [39], with a selection catered to the specific b' model by tagging b-jets using displaced vertices.

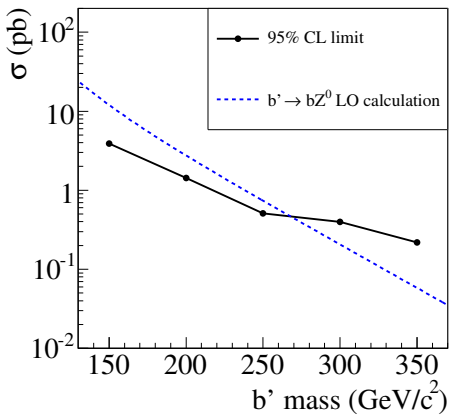

Figure 5.39: Cross section limit vs. b' mass, set at a confidence level of 95%. In the acceptance calculation $BR(b' \rightarrow bZ) \equiv \beta = 100\%$ was assumed. If $\beta < 100\%$, the acceptance would scale by the factor $1 - (1 - \beta)^2$, since the b' is produced in pairs and only one of them is required to decay to a Z with our selection. In addition, non-Z decays could change the acceptance of the $N_{\rm jet}^{30} \geq 3$ cut.

b' mass (GeV)	Acceptance (%)
150	1.05
200	1.44
250	1.61
300	1.66
350	1.77

Table 5.8: Acceptances to select $b' \to bZ$ events versus mass, after applying the $N_{\text{jet}}^{30} \geq 3$ and $J_T^{30} > m_{b'}c^2$ requirements. These include a factor from the branching ratio of $Z \to ee$ and $Z \to \mu\mu$. If this factor is removed, the acceptances range from 8–14%. $BR(b' \to bZ) = 100\%$ was assumed.

Chapter 6

Conclusion

I have described all of my efforts made during my graduate career of trying to find physics beyond the standard model. Unfortunately, there was no evidence of new physics. Rather, only limits on possible new particles.

I presented the results of a search for new long-lived particles decaying to Z bosons. No significant excess was found, and so limits were set on the b' model as a function of lifetime.

I also presented the results of a search for new particles decaying to Z bosons and jets. Again, there was no significant excess, and so a limit was set, again on the b' model, but with a short-lived assumption. The two analyses complement each other.

For the Z+jet search, I (with the help of my colleagues) developed and validated a new technique to predict the dominant background from the data alone. This technique is an alternative to the phenomenological-based method of predicting backgrounds via Monte Carlo calculations of higher-order matrix elements and non-perturbative soft parton showers. The technique has advantages of not requiring careful tuning of phenomenological parameters when comparing to data, and not requiring the many resource-consuming iterations of Monte Carlo detector simulations. The speed with which it can be applied makes it an attractive tool for calculation of backgrounds in jet-rich environments at future experiments, including those at the Large Hadron Collider.

After developing and validating this technique, I have gained an intuition for it, understanding its limitations and opportunities for refinements. I would like to mention them here, for others that may wish to use and improve this method in the future.

In the J_T shape prediction, a single parameter extrapolation was used to estimate the jet E_T shapes at high $N_{\rm jet}$ from those at high $N_{\rm jet}$. This could be enhanced by developing a more sophisticated method of extrapolating both jet E_T shape parameters simultaneously. In addition, in the extrapolation, the assumption that the jet E_T's are uncorrelated was made. While this assumption

was seen to not have a significant effect on the extrapolation, allowing for a correlation somehow would make the procedure more theoretically satisfying.

The fits of the jet E_T distributions might be enhanced if the parameterization used can be constrained with phenomenological guidance. Right now, the exponential parameter (p_1) and the power law parameter (p_2) are allowed to float independently. It may be that knowledge of one might constrain the other. If this were true, this would enhance the power of the technique a great deal. If they are related, the power law parameter could be found by a fit to the lower part of the E_T distribution (where a power law dominates), allowing for a measurement of the exponential parameter, and thus a measurement of the high E_T portion of the distribution. A detailed phenomenological understanding of the jet E_T shape might help answer this question.

Appendix A

Jet E_T Parameterization

In order to fit the jet E_T distributions, we need a parameterization that models the essential features of those distributions well. In the following, we use Z+jet Monte Carlo as a guide to determine the correct parameterization, although the parameterization found here is validated from our studies in data. In Fig. A.1, we show the highest jet E_T distribution on a semi-log plot. At high E_T, the distribution appears to have an exponential dependence. In Fig. A.2, we show the same distribution, but on a log-log plot. At low E_T (but above the turn-on), the distribution appears to have a power-law dependence. We therefore seek

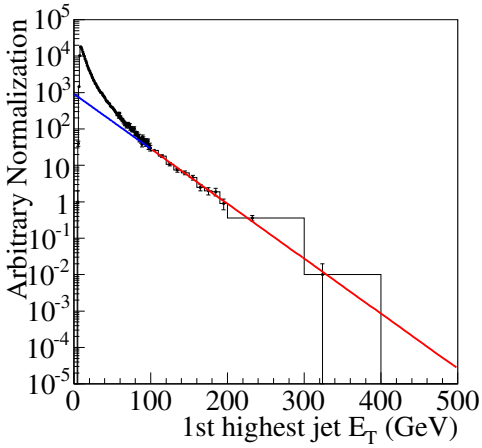

Figure A.1: E_T distribution of the highest E_T jet in standard model $Z \rightarrow \mu\mu$ Monte Carlo. The distribution is fit to an exponential in the range $E_T >$ 100 GeV.

a parameterization which behaves as an exponential at high E_T, and a power law at low E_T. The following parameterization satisfies this requirement:

$$f(E_T) = p_0 \frac{e^{-E_T/p_1}}{(E_T)^{p_2}} \tag{A.1}$$

With the parameterization written this way, the parameter p_1 has dimensions of energy, the parameter p_2 is dimensionless, and both parameters are positive. We fit the same distribution in Figs. A.1 and A.2 to this parameterization in Fig. A.3. This parameterization indeed models the essential features of this distribution well.

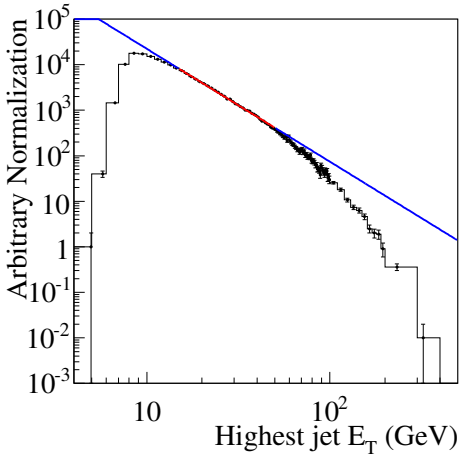

Figure A.2: Same distribution as figure A.1, fit to a power law in the range $15 < E_T < 50$ GeV.

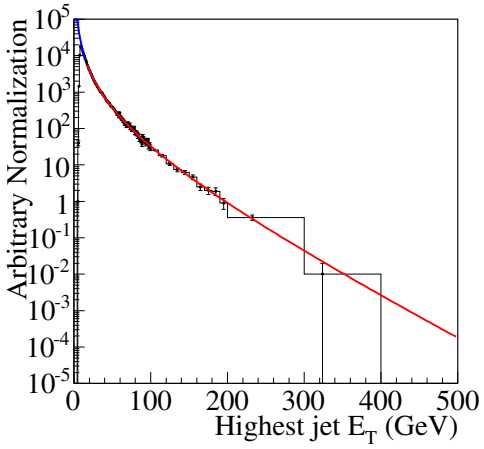

Figure A.3: Same distribution as figure A.1, fit to the parameterization in Eq. (A.1) in the range $E_T > 15$ GeV.

We have verified that this parameterization also describes the jet E_T distribution in various control samples, including blinded Z+jet data and jets in QCD-rich dijet samples as described in Sec. 5.4.4. While it is difficult to determine the expected shape of the E_T distribution of jets in standard model Z events from phenomenological first principles, we can easily determine the shape of a different but related quantity. Consider the Feynman diagram in Fig. A.4, in which two partons collide to form a virtual particle with zero pole-mass. The related quantity we calculate is the invariant mass distribution of the virtual particle, given the distributions of the parton momenta k_1 and k_2. The four-momenta (which include the superscript "(4)" in our notation) of the incoming partons are, neglecting their masses:

$$\begin{aligned} k_1^{(4)} = &\quad (E_1, k_1) &&\simeq (k_1, k_1) \\ k_2^{(4)} = &\quad (E_2, -k_2) &&\simeq (k_2, -k_2) \\ k_3^{(4)} = &\quad (E_3, k_3) &&= (\sqrt{m_3^2 + k_3^2}, k_3) \end{aligned}$$

Note, since we are not necessarily in the CM frame, $k_1 \neq k_2$. Using four-momentum conservation:

$$\begin{aligned} k_1^{(4)} + k_2^{(4)} &= k_3^{(4)} \\ (k_1 + k_2, k_1 - k_2) &= (\sqrt{m_3^2 + k_3^2}, k_3) \end{aligned}$$

From these two simultaneous equations (one equation for each component) m_3 can be obtained in terms of k_1 and k_2:

$$m_3 = \sqrt{(k_1 + k_2)^2 - (k_1 - k_2)^2}$$

So, if we are given k_1 and k_2, we can find m_3. At a hadron collider, k_1 and k_2 are sampled from the parton distribution functions (PDFs). We now wish to determine the shape of m_3 given an estimate of the shapes of the incoming parton momenta. For a rough estimate of this, we take only the $u + \bar{u}$ PDF. We use the parameterization given in [27], Eq. (4), and the parameter values for the $u + \bar{u}$ PDF. (These values are taken from Appendix A of [27], assuming $\bar{u} = \bar{d}$ in the proton—an incorrect but close approximation). We show the PDF of these partons in Fig. A.5. Since we have the distribution of the momenta of the partons (the PDF), and an equation relating the momenta of the partons to the combined particle, we have all we need to construct a simple Monte Carlo to get the distribution of m_3. We simply generate values of k_1 and k_2 from the PDF (with a total beam energy of ~ 1 TeV), and use the above equation to get m_3. Of course, the generic behavior of cross sections is $\sigma \sim 1/s$, so we must weight each event by $1/m_3^2$. We show the distribution of m_3 from such a Monte Carlo in Fig. A.6, with a fit to the parameterization in Eq. A.1. For a large range of the distribution, the parameterization describes the shape of m_3 adequately. As

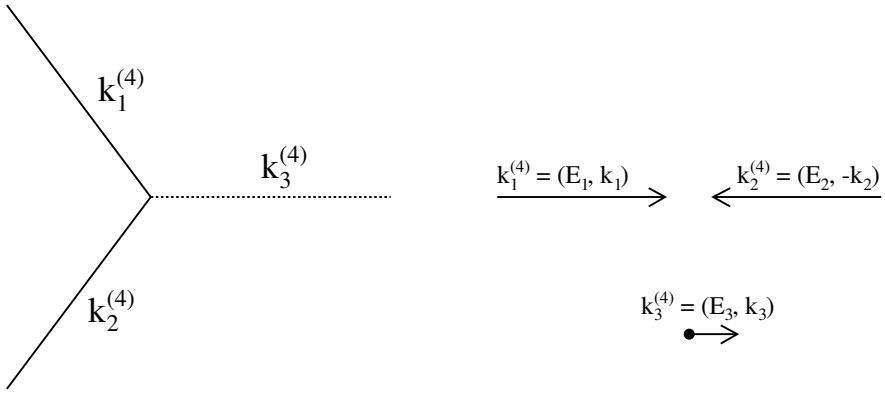

Figure A.4: Two partons from a proton and anti-proton colliding.

our chosen parameterization matches what is seen in Monte Carlo and observed in control regions of data, and as it models the shape of this related quantity, we are confident that it sufficiently describes the jet E_T distribution.

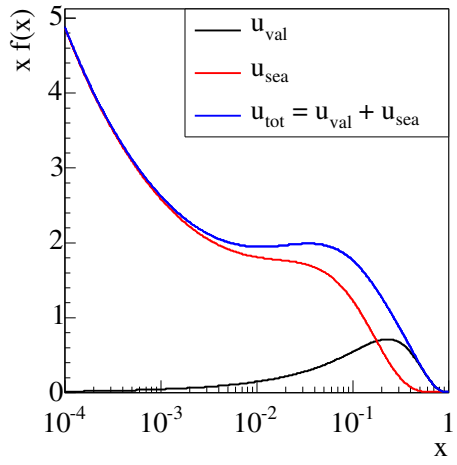

Figure A.5: Parton distribution function from [27].

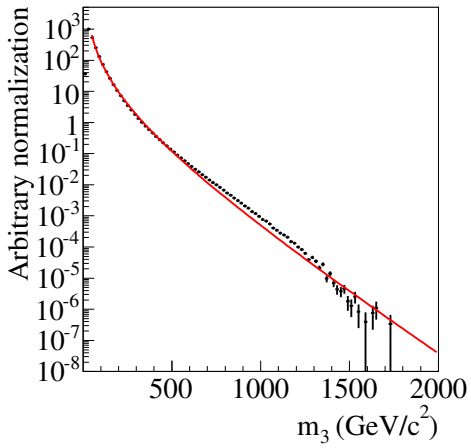

Figure A.6: Output of a simple Monte Carlo describing the process in figure A.4. The distribution is fit to the parameterization in Eq. (A.1).

Bibliography

[1] The following references have helped me to understand the standard model and quantum field theory, and they will hopefully help those wishing to learn it from scratch. Unfortunately, they are no substitute for a course taught by a good professor.

L. S. Brown, "Quantum Field Theory," *Cambridge, UK: Univ. Pr. (1992).*

F. Mandl and G. Shaw, "Quantum Field Theory," *Chichester, Uk: Wiley (1984) (A Wiley-interscience Publication).*

M. E. Peskin and D. V. Schroeder, "An Introduction To Quantum Field Theory," *Reading, USA: Addison-Wesley (1995).*

D. J. Griffiths, "Introduction To Elementary Particles," *New York, USA: Wiley (1987).*

M. Srednicki, hep-th/0409035 and hep-th/0409036.

[2] R. Cahn, Rev. Mod. Phys. **68** 951 (1996).

[3] P. Langacker, Phys Rep. **72** 185 (1981).

[4] W.-M. Yao et al. (Particle Data Group), J. Phys. G **33**, 1 (2006), p119-137.

[5] G. Burdman, hep-ph/0703194.

[6] S. P. Martin, hep-ph/9709356.

[7] W. Pauli, Phys. Rev. **58**, 716 (1940).

[8] C. S. Wu, E. Ambler, R. W. Hayward, D. D. Hoppes and R. P. Hudson, Phys. Rev. **105**, 1413 (1957).

R. L. Garwin, L. M. Lederman and M. Weinrich, Phys. Rev. **105**, 1415 (1957).

[9] S. B. Giddings and S. D. Thomas, Phys. Rev. D **65**, 056010 (2002).

[10] N. Arkani-Hamed, S. Dimopoulos and G. R. Dvali, Phys. Lett. B **429**, 263 (1998).

[11] J. Polchinski, "String theory. Vol. 1: An introduction to the bosonic string," *Cambridge, UK: Univ. Pr. (1998).*

J. Polchinski, "String theory. Vol. 2: Superstring theory and beyond," *Cambridge, UK: Univ. Pr. (1998).*

[12] P.H. Frampton, P.Q. Hung, and M. Sher, Phys. Rept. **330**, 263 (2000).

[13] D. Acosta et al. [CDF Collaboration], Phys. Rev. D **71**, 031104 (2005).

V. M. Abazov et al. [D0 Collaboration], Phys. Rev. Lett. **94**, 041801 (2005).

[14] G. Anderson et al., Phys. Rev. D **61**, 095005 (2000).

[15] S. Ambrosanio et. al., Phys. Rev. D **54** 5395 (1996).

[16] P. Wagner and D. A. Toback, Int. J. Mod. Phys. A **20**, 3267 (2005).

[17] H. T. Edwards, Ann. Rev. Nucl. Part. Sci. **35**, 605 (1985).

D.P. McGinnis, "FNAL Tevatron operational status", Proceedings of the Particle Accelerator Conference (PAC 05) (2005).

[18] Pbar note #683, `http://www-bdnew.fnal.gov/pbar/documents/pbarnotes/pdf_files/pb683.pdf`

[19] J. B. Rosenzweig, A. M. Cook, A. Scott, M. C. Thompson, and R. B. Yoder, Phys. Rev. Lett. **95**, 195002 (2005).

[20] M.C. Thompson, H. Badakov , J.B. Rosenzweig , G. Travish , M. Hogan, R. Ischebeck, N. Kirby, R. Siemann, D. Walz, P. Muggli, A. Scott, and R. Yoder, AIP Conf. Proc., **877**, 903 (2006).

[21] J. Seeman, Ann. Rev. Nucl. Part. Sci. **41** (1991) 389.

[22] Katsouleas, T. Phys. Rev. A. **33**, 2056 (1986).

[23] D. Acosta, et al. [CDF Collaboration], Phys. Rev. D **71**, 032001 (2005).

C.S. Hill, Nucl. Instrum. Methods A **530**, 1 (2004).

A. Sill, et al., Nucl. Instrum. Methods A **447**, 1 (2000).

A. Affolder, et al., Nucl. Instrum. Methods A **453**, 84 (2000).

T. Affolder et al., Nucl. Instrum. Methods A **526**, 249 (2004).

D. Acosta et al., Nucl. Instrum. Methods A **518**, 605 (2004).

L. Balka, et al., Nucl. Instrum. Methods A **267**, 272 (1988).

S.R. Hahn, et al., Nucl. Instrum. Methods A **267**, 351 (1988).

S. Bertolucci, et al., Nucl. Instrum. Methods A **267**, 301 (1988).

M. Albrow et al., Nucl. Instrum. Methods A **480**, 524 (2002).

G. Apollinari et al., Nucl. Instrum. Methods A **412**, 515 (1998).

G. Ascoli et al., Nucl. Instrum. Methods A **268**, 33 (1988).

T. Dorigo et al., Nucl. Instrum. Methods A **461**, 560 (2001).

D. Acosta et al., Nucl. Instrum. Methods A **494**, 57 (2002).

W. Ashmanskas, et al., Nucl. Instrum. Methods A **518**, 532 (2004).

E.J. Thomson, et al., IEEE Trans. on Nucl. Science **49**, 1063 (2002).

[24] D. Acosta et al., Nucl. Instrum. Methods Phys. Res. A **494** 57 (2002).

S.Klimenko, J. Kongisberg, and T.M. Liss, FERMILAB-FN-0741

[25] T. Sjostrand et al., Comput. Phys. Commun. **135**, 238 (2001). PYTHIA version 6.216

[26] R. Brun and F. Carminati, CERN Programming Library Long Writeup W5013 (1993). GEANT version 3.21/14 was used.

[27] J. Pumplin, D. R. Stump, J. Huston, H. L. Lai, P. Nadolsky and W. K. Tung, JHEP **0207**, 012 (2002) [arXiv:hep-ph/0201195].

[28] S. Ambrosanio et al., Phys. Rev. D **54**, 5395 (1996).

[29] J. D. Bjorken, S. Pakvasa, and S. F. Tuan, Phys. Rev. D **66** 053008 (2002).

[30] M.J. Strassler and K.M. Zurek, arXiv:hep-ph/0605193.

[31] M. Krämer, S. Mrenna, and D.E. Soper, Phys. Rev.D **73** 014022 (2006).

[32] S.D. Ellis et al., eConf **C010630** P513 (2001), [arXiv:hep-ph/0111434].

[33] A. Bhatti et al., Nucl. Instrum. Methods Phys. Res. A **566**, 375 (2006).

[34] G. Punzi, *In the Proceedings of PHYSTAT2003: Statistical Problems in Particle Physics, Astrophysics, and Cosmology, Menlo Park, California, 8-11 Sep 2003, pp MODT002* [arXiv:physics/0308063].

[35] W.-M. Yao et al. (Particle Data Group), J. Phys. G **33**, 1 (2006), p528.

[36] D. Acosta et al. [CDF Collaboration], Phys. Rev. D **72**, 052003 (2005).

[37] Section 4 of J. Conway, *Proceedings of Workshop on Confidence Limits, Geneva, Switzerland, 17-18 Jan 2000*, FERMILAB-CONF-00-048-E

[38] A. Abulencia et al. [CDF Collaboration], FERMILAB-PUB-05-360-E [arXiv:hep-ex/0508029].

[39] T. Affolder et al. [CDF Collaboration], Phys. Rev. Lett. **84**, 835 (2000).